A Coherent Method for Denoising Ultrasound Data with Applications in Super Resolution and Elastography

Parviz Khavari

A Thesis

in

The Department

of

Electrical and Computer Engineering

Presented in Partial Fulfillment of the Requirements

for the Degree of

Master of Applied Science (Electrical and Computer Engineering) at

Concordia University

Montréal, Québec, Canada

August 2018

CONCORDIA UNIVERSITY

School of Graduate Studies

This is to certify that the thesis prepared

By: **Parviz Khavari**

Entitled: **A Coherent Method for Denoising Ultrasound Data with Applications in Super Resolution and Elastography**

and submitted in partial fulfillment of the requirements for the degree of

Master of Applied Science (Electrical and Computer Engineering)

complies with the regulations of this University and meets the accepted standards with respect to originality and quality.

Signed by the final examining committee:

_____ Chair
Dr. Dongyu Qiu

_____ Examiner
Dr. Abbas Javadtalab

_____ Examiner
Dr. Reza Soleymani

_____ Thesis Supervisor(s)
Dr. Amir Asif

_____
Dr. Hassan Rivaz

Approved by

_____
Dr. William E. Lynch, Chair
Department of Electrical and Computer Engineering

_____
Dr. Amir Asif, Dean
Faculty of Engineering and Computer Science

Date: 14 August 2018

Abstract

A Coherent Method for Denoising Ultrasound Data with Applications in Super Resolution and Elastography

Parviz Khavari, M.A.Sc.

Concordia University 2018

Ultrasound (US) imaging is a widely used medical modality since it is inexpensive non-invasive and portable. However, the quality of US is limited by physical constraints (e.g. thermal noise) and hardware restrictions (e.g. the number of sensors in a US probe). To increase the quality and improve the resolution of US images, I proposed two novel algorithms, namely COherent Denoising for Elastography (CODE), for removing noise of RF data for elastography technique and coherent ultrasound super-resolution to perform a novel super-resolution technique.

I first propose CODE to improve the estimation of tissue displacement in ultrasound elastography. Ultrasound elastography computes the mechanical properties of tissues affected by an internal of external force. The radio frequency data acquired from ultrasound is usually corrupted with noise that leads ultrasound elastography techniques for fail. To remove this noise I proposed CODE that despite the local denoising algorithms, keeps the information of the RF data for elastography. I investigate two state-of-the-art elastography methods, GLobal Ultrasound Elastography (GLUE), and; (ii) Dynamic Programming Analytic Minimization elastography, and results shows the improvement of the strain maps on both patient and phantom data.

I then introduce a super-resolution technique for improving the quality of ultrasound B-mode images. The resolution of ultrasound images is limited by hardware constraints and physical restrictions. Conventionally, ultrasound machines use interpolation techniques for improving the resolution of the B-mode images. However, I propose a new method for coherent ultrasound super-resolution that overcomes conventional approaches in both qualitative and quantitative measures.

In both cases, I proposed a mathematical framework that justified the behavior of the algorithms

and tested the methods on both *in-vivo*, and phantom data, and discussed qualitatively and quantitatively.

Acknowledgments

First and foremost, my acknowledgement goes to my erudite supervisors, Prof. Amir Asif and Prof. Hassan Rivaz, for their guidance and support for my research. Their novel ideas, accurate leading, and precise review were irreplaceable opportunity I had throughout my study, and I am sincerely thankful for this unique opportunity.

Moreover, I would love to thank my beloved mom, dad, brother and girlfriend for their pure love and warm support. Also I do deeply appreciate my friends and coleagues in Concordia University, and IMPACT lab for their fruitful opinions and rewarding discussions, especially Mr. Hossein Khodadadi. I would like to thank Julian Lee from Alpinion USA for technical help.

This research has been supported by NSERC Discovery grants RGPIN-2015-04136 and RGPIN-2017-06629.

to my beloved parents and brother

Contents

List of Figures

List of Tables

Chapter 1

Introduction

In this chapter, I review the basics of ultrasound and the physical rules that make the ultrasound imaging possible. After talking about foundation of this modality, I investigate two applications in ultrasound imaging included ultrasound elastography and ultrasound super resolution that both have different usages in medical diagnosis. Finally at the end, I conclude the chapter by the outlines of this thesis and the journal and conference publication that have been accepted and published recently.

1.1 Ultrasound Physics

In this section, I review the principles of ultrasound imaging. After studying the physics of ultrasound, I review the kind of probes that are using for ultrasound imaging. At PERFORM center, IMPACT laboratory has two ultrasound machines, with access to raw research data that makes it among the best well-equipped research laboratories worldwide. Ultrasound is acoustic waves with the frequencies of above 20 KHz. The commercial ultrasound machine frequency is in the range of 1 MHz to 20 MHz. Ultrasound imaging is widely used modality since it is in-expensive, portable, non-invasive and non-ionizing imaging modality and has numerous application in diagnostic, operations and even treatment. It consists of a probe with array of piezoelectric transducers, that each piezoelectric can trig and receive the acoustic wave. The probe usually is place on the special surface of tissue without any air gap between, to scan the tissue underneath of the probe. To remove

the gap of air between tissue and probe, the surface of tissue is covered with ultrasound water-based gel.

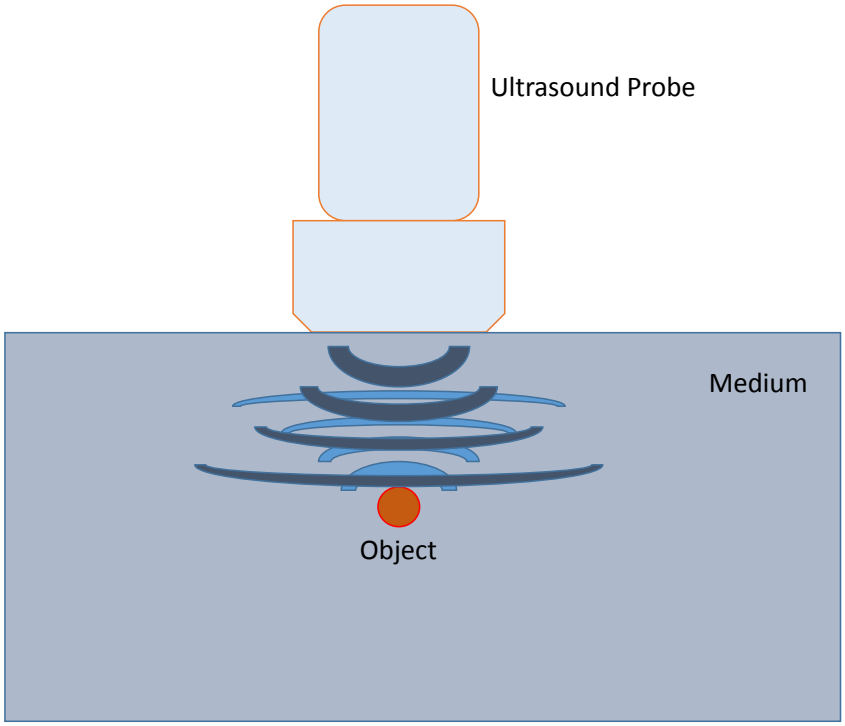

Figure 1.1: The emitted wave (dark blue wave) from ultrasound hits the object and reflects toward ultrasound probe (pale blue wave)

Then, an ultrasound wave is submitted through the probe and a portion of wave is reflected back to the probe. There are three main kind of probes that ultrasound machines are using for imaging the tissue. The reflected signals (a.k.a. echoes) are then converted to the electrical voltage and this electrical voltage, in the literature of ultrasound is known as Radio Frequency (RF) data. The RF data is not suitable for visualization, therefore, by computing the envelope of RF data, the B-mode images are introduced that are the main outputs of ultrasound machines. The difference between amplitude of B-mode images is showing the different between acoustic properties of the tissue. In the B-mode image, each pixel is represented by the back-scatterer amplitude from that part of tissue. Speckles Rivaz et al. (2006), are the results of interference of different back-scatterers in

Figure 1.2: Alpinion E-cube 15R at the PERFORM Centre

the ultrasound B-mode are the main factor in grainy appearance of the B-mode. The speckles are reproducible, that means if you scan a certain area of tissue separately, it leads to the same speckle pattern. This property leads to a new cater gory of methods for computing the stress of the tissue by information of speckles from RF raw data. This extracting the mechanical properties of tissue is also known ultrasound elastography. Figure 1.2 shows that Alpinion Ultrasound machine that provides radio frequency data that has been used in this thesis.

1.2 Ultrasound Elastography

Elastography algorithms can be categorized into two main group of dynamic and quasi-static elstography Gao et al. (2017); Hamaluik et al. (2014); Ouared et al. (2015); Papadacci et al. (2017). In quasi-static elastography, the tissue is deformed using an external force and the force creates a displacement map (See Figure 1.3). But in dynamic elstography, by using the features of wave

induced by probe, Figure 1.4, the mechanical property of tissue is deciphered.

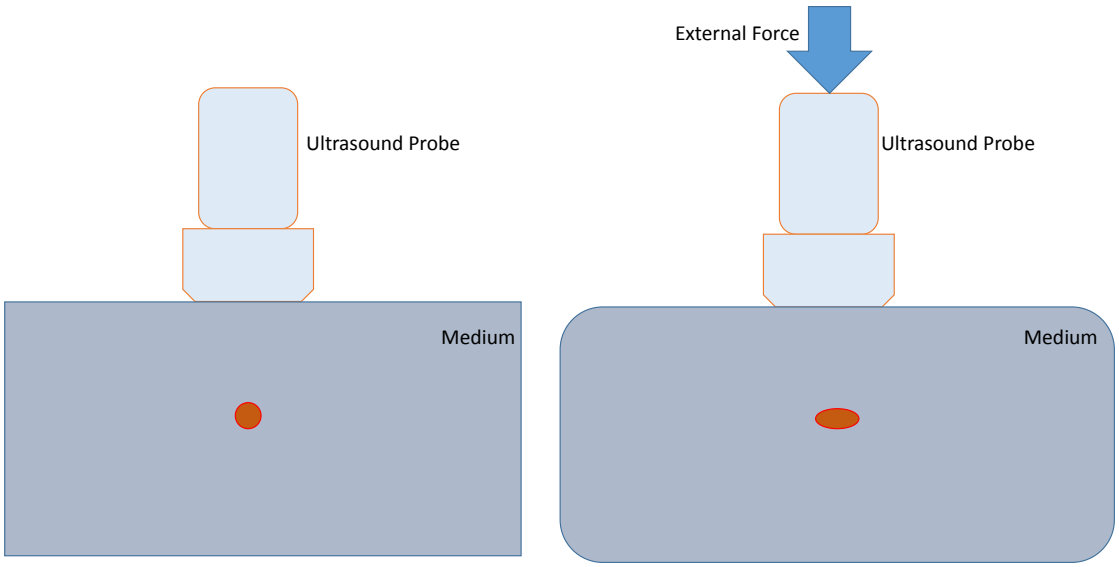

Figure 1.3: Illustration of quasi-static elastography by external force of a probe

The differentiating of displacement map produce the strain field of the tissue that contains the information of stiffness and flexibility of the tissue. In dynamic elastography, an acoustic wave, shear wave, propagates through the tissue and the mechanical properties of tissue is calculated quantitatively. More comprehensive study of dynamic elastography and quasi-static elastography can be found in Doyley (2012)and Ophir et al. (1999).

As mentioned, in quasi-static elastography the displacement map is necessary for computing the strain. A popular approach for obtaining the displacement field is to define a cost function and based on dynamic approach, try to solve the inverse problem. This method has been used in several publications, Hashemi and Rivaz (2017); Rivaz et al. (2011), namely GLobal Ultrasound Elastography (GLUE) and Dynamic Programming Analytic Minimization elastography (DPAM), respectively. The advantage of this approaches is high resolution in lateral direction, despite the intrinsic property of ultrasound that the resolution in lateral is poor, and high computing efficiency. But a drawback of these method is that they are vulnerable to the selecting seed line, that is a line selected in both cases to compute the integer displacement for a line to form the displacement map.

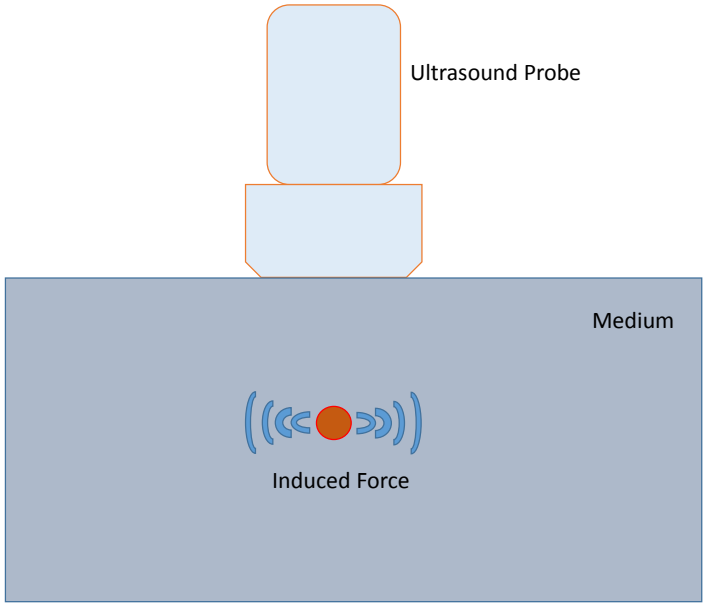

Figure 1.4: Illustration of dynamic elastography by induced force of probe

In very noisy applications, such as liver ablation, the noise leads algorithms to fail, because the seed line displacement calculation is failed.

For improving elastography in ultrasound, I present a novel approach called COherent Denoising for Elastography, CODE, that address this issue and improved the output RF signal in sense of Sum of Absolute Difference (SSD), Chi Squared and Normalized Root Mean Square Error (NRMSE) followed by mathematical frame work that explain the efficiency of CODE.

1.3 Super Resolution

Another intrisic problem of ultrasound imaging, that is poor quality of images is also addressed in this thesis. To improve the quality, I proposed a novel iterative algorithm supported with a Bayesian framework, that creates better B-mode images with higher quality. The method has decreased the residual pattern between ground truth and regenerated high resolution images by 50% that confirms the advantage of proposed method in compare with conventional methods to increase

the resolution of B-mode images. Some of RF data are collected at PERFORM center. Figure 1.5 shows the collection of RF data from ultrasound phantom. Figure 1.6 shows the improvement of the resolution of a B-mode image using proposed technique.

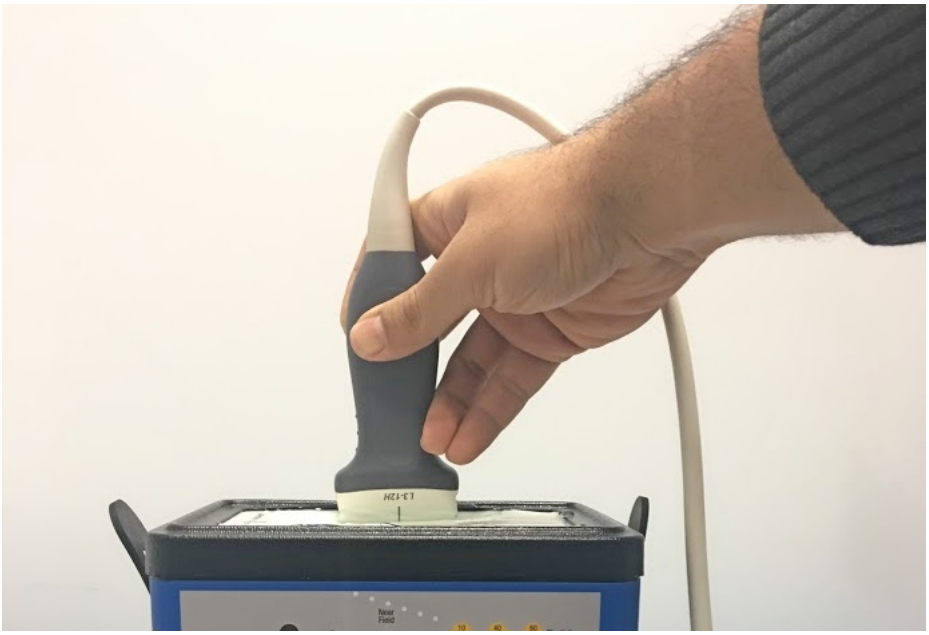

Figure 1.5: Collection of ultrasound RF data from a commercial tissue-mimicking phantom.

Field II is a program for simulation of ultrasound imaging with setting the parameters of ultrasound simulation, e.g. central frequency, sampling frequency etc. The program is able to calculate the emitted pulse and received echo of continuous wave for a variety of different transducers Wood et al. (1999). The program is running on matlab and currently is free to use Jensen (1999).

1.4 Outline of Thesis

In Chapter 2, the author introduces a novel coherent denoising approach, CODE, for removing the noise in ultrasound imaging. CODE can remove the noise while keeping the pattern of speckles using for post processing algorithms, e.g. elastography algorithm. The denoised RF data of ultrasound is used for elastography using two different methods, GLUE Hashemi and Rivaz (2017) and DPAM Rivaz et al. (2011). Followed by mathematical framework that confirms the effectiveness of

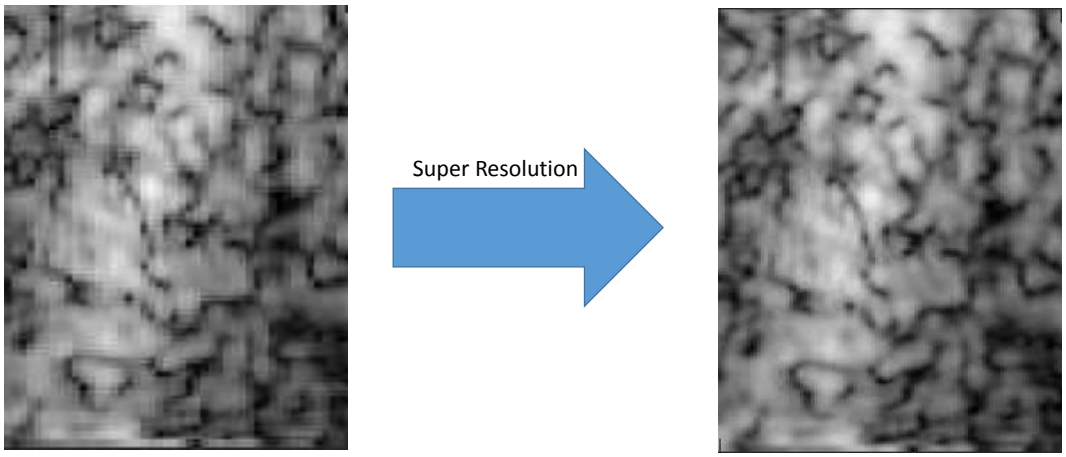

Figure 1.6: Proposed super resolution technique improves the resolution in B-mode ultrasound images.

CODE, the results of clinical patients (in a noisy environment of liver ablation) and phantom data affirms the superiority of CODE in compare with other denoising algorithms on RF data and B-mode images. However, further clinical study is needed to support the results of CODE to investigate more aspects of proposed algorithm in this chapter for real-world application.

The results of this chapter have been published as an invited research journal paper in Journal of Healthcare Engineering, 2018.

In Chapter 3, a novel algorithm for ultrasound super resolution imaging is proposed. The algorithm is supported by a Bayesian framework for more insight of performance of the algorithm. The proposed algorithm is compared with conventional methods for enhancing the resolution of ultrasound B-mode images, and the results of studying clinical patient data and phantom data demonstrate the advantages of the proposed algorithm in contrast with other established method. This chapter is concluded by addressing future works and remarks. This Chapter has been published as a research conference article in IEEE MultiMedia Signal Processing (MMSP 2018).

1.5 Publications

The results of this master's thesis are accepted for a journal and conference which are listed as items below.

- P. Khavari, A. Asif, M. Boily and H. Rivaz,*"Non-Local Coherent Denoising Of RF Data For Ultrasound Elastography"*, Invited Paper to Hidawi Journal of Healthcare Engineering Khavari et al. (2018)

- P. Khavari, A. Asif and H. Rivaz, *"Non-Local Super Resolution in Ultrasound Imaging"*, IEEE Multimedia Signal Processing Conference (MMSP), Aug 2018

Chapter 2

Coherent Nonlocal Filtering for Elstography

2.1 Overview

Ultrasound elastography infers mechanical properties of living tissues from ultrasound radio frequency (RF) data recorded while the tissues are undergoing deformation. A challenging yet critical step in ultrasound elastography is to estimate the tissue displacement (or, equivalently the time delay estimate) fields from pairs of RF data. The RF data is often corrupted with noise, which causes the displacement estimator to fail in many *in-vivo* experiments. To address this problem, I present a non-local, coherent denoising approach based on Bayesian estimation to reduce the impact of noise. Despite incoherent denoising algorithms that smooth the B-mode images, the proposed denoising algorithm is used to suppress noise while maintaining useful information such as speckle patterns. I refer to the proposed approach as COherent Denoising for Elastography (CODE) and evaluate its performance when CODE is used in conjunction with two state-of-art elastography algorithms, namely: (i) GLobal Ultrasound Elastography (GLUE), and; (ii) Dynamic Programming Analytic Minimization elastography (DPAM). Our results show that CODE substantially improves the strain result of both GLUE and DPAM.

2.2 Introduction

Ultrasound elastography determines the viscoelastic properties of tissues, and is useful for diagnosis of pathology and for aiding surgeons in the operating room. Broadly speaking, ultrasound elastography can be grouped into two categories Ophir et al. (1999)-Tang et al. (2015): dynamic elastography and quasi-static elastography. In this chapter, I focus on two state-of-art free-hand palpation, quasi-static elastographic approaches, namely Global Time-Delay Estimation in Ultrasound Elastography (GLUE) Hashemi and Rivaz (2017) and Real-Time Regularized Ultrasound Elastography (DPAM) Rivaz et al. (2011). Both approaches use successive pairs of frames of ultrasound RF data to estimate the tissue displacement (also referred to as time delay estimates (TDE)). The derivative of TDE provides an estimate of the induced strain that represents the stiffness or softness of the tissue being imaged. Figure 2.1 illustrates the steps involved in quasi-static ultrasound elastography with the hand-held device shown on the left hand-side and the displacement field estimates defined using the two frames on the right.

At the heart of both GLUE and DPAM is an energy minimization approach to determine TDE's . A dynamic programming approach is used in both cases to compute TDE's first at a coarse pixel level. The resolution of the TDE's is then enhanced to the finer sub-pixel level through analytical minimization. Given that RF ultrasound data can be corrupted by several factors such as thermal and electronic noise, there is a need to compensate for noise in the RF data. Traditional filtering techniques, such as the convolution with a Gaussian kernel, use local continuity in the images to reduce noise. A new class of denoising algorithms, referred to as non-local means (NLM) Buades et al. (2005), considers data from a much larger "non-local" region for denoising. NLM relies on redundancy in images and uses the weighted average of most similar intra-frame pixels within a large non-local neighbourhood to eliminate noise.

Most NLM based denoising approaches Coupé et al. (2009); Kervrann et al. (2007); Khodadadi et al. (2015) remove noise from processed output of the RF data, which is referred to as B-mode images in ultrasound literature. NLM denoising reduces speckle pattern and generates smooth B-mode images. Ultrasound speckle is useful in several image analysis techniques, such as ultrasound elastography Ophir et al. (2002); Rivaz et al. (2014), freehand sensor-less 3D ultrasound Afsham

et al. (2014); Rivaz et al. (2007) and quantitative ultrasound Oelze and Mamou (2016). In this work, I focus on ultrasound elastography.

In this chapter, I present an alternate approach wherein NLM denoising algorithm is applied directly to raw RF data instead of processed B-mode images. I refer to the proposed approach as COherent Denoising for Elastography (CODE) and evaluate its performance on *in-vivo* liver ablation data when used in conjunction with two commonly used elastography algorithms, namely: (i) GLobal Ultrasound Elastography (GLUE) Hashemi and Rivaz (2017), and; (ii) Dynamic Programming Analytic Minimization elastography (DPAM) Rivaz et al. (2011). CODE exploits the complete set of information in the RF domain, some of which is likely to be lost in the processing steps used to generate the B-mode images. It is, therefore, our intuition that CODE would result in superior denoising results. Using information in RF data to generate visually informative B-mode images is challenging Wachinger et al. (2012). To illustrate the superiority of CODE, both mathematical analysis and experimental results are included in the chapter. Our comparisons corroborate our intuition and verify the usefulness of CODE.

The rest of this chapter is organized as follows. In Section 2.3, I review GLUE and DPAM as representative quasi-static elastography approaches. Section 2.4 provides background on non-local denoising and introduces CODE as a Bayesian estimator. In Section 4, I explore the ability of CODE on simulation data. Experimental results using phantom and *in-vivo* data are included in Section 5. Finally, I conclude the chapter in Section 6.

2.3 Quasi-static Elastography: GLUE and DPAM

Both DPAM and GLUE are quasi-static approaches based on the optimizing a regularized cost function to determine tissue displacements. They both aim at finding the axial and lateral displacements (a and l) of all samples of RF data as shown in Figure 2.1. DPAM uses dynamic programming (DP) to first estimate the integer displacement of a *seed-line* in terms of the number of pixels and then applies analytical minimization (AM) to fine tune the estimated displacement to the sub-pixel level. The strain image is obtained using the spatial differentiation of the displacement field. GLUE also uses DP for estimating the integer tissue displacements and refines the estimates to sub-pixels

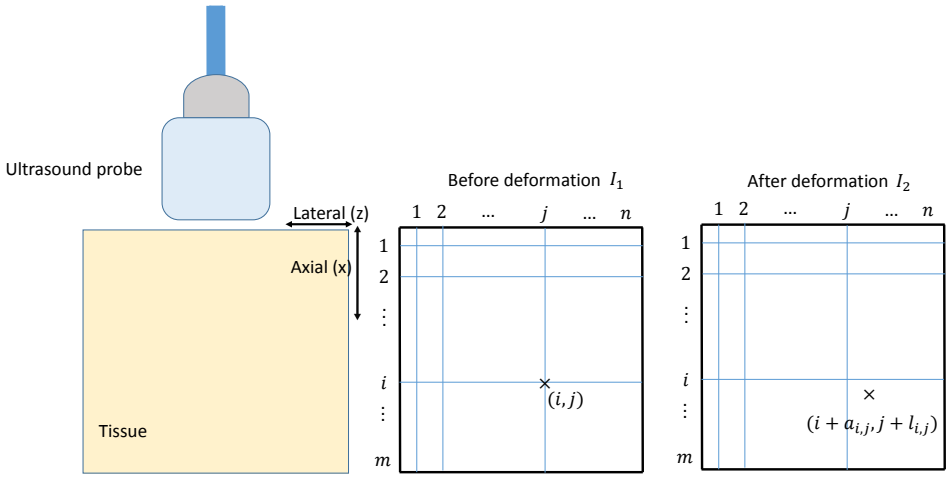

Figure 2.1: Illustration of ultrasound elastography. The left figure shows a hand-held device that induces an external stimulus into the tissues. The pair of figures on the right include two successive frames I_1 and I_2 of RF data. The goal of ultrasound elastography is to find the displacement $(a_{i,j}, l_{i,j})$ for each pixel (i, j) in the I_1 RF frame.

for the entire image simultaneously. In other words, GLUE solves an optimization function where both axial and lateral displacement of every sample of the RF frame are unknowns, i.e. in the order of a million variables. This is in contrast to DPAM, which refines the estimates line-by-line. The strain image again is calculated based on the differentiation of displacement map similar to DPAM. Although GLUE and DPAM perform well in most cases, they may not converge to the correct solution in the presence of excessive noise. In the next section, I present our denoising approach used to reduce the impact of noise in the RF domain.

2.4 The NON-local Denoising Approach

The central idea behind this chapter is to apply coherent denoising on RF data. Unlike incoherent denoising approaches that process the B-mode images to remove noise (resulting in spatial averaging and significant loss of speckle patterns), the proposed approach retains speckle patterns. I first outline NLM, which followed by a description of the CODE algorithm, including an analytical justification of why CODE provides better denoising results.

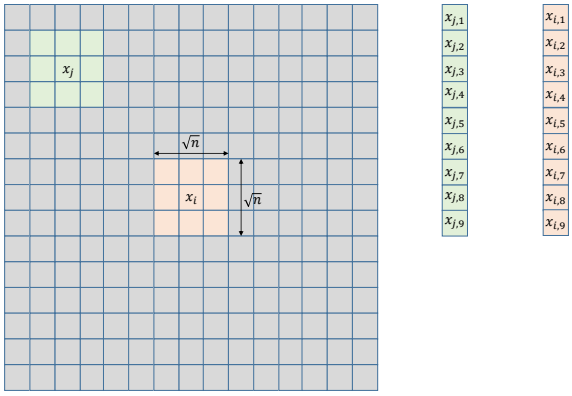

Figure 2.2: Illustration for the patch and vectorized indices used in the proposed CODE approach for $n = 9$.

2.4.1 Non-local means

Let $v(i)$ be the observed value of the discretized image for pixel i and $u(i)$ be its true value. Due to the presence of noise $n(i)$, I have

$$v(i) = u(i) + n(i). \tag{1}$$

To simplify our explanation, I focus on 1D signals but our results are generalizable to 2D images. In fact, the experimental results included in Section 4 are for 2D phantom and in-vivo liver ablation data. To denoise the image for each pixel i, NLM searches a reference area of the image within a rectangular *search window* Δ_i, which is centered around pixel i (see Figure 3.2). A neighbourhood N_i of known dimension is selected around pixel i and compared to neighbourhood N_j around pixel j for all $j \in \Delta_i$. For pixel i, weight $w(i, j)$ is assigned to each pixel j. The value of pixel i is then replaced by

$$\text{NLM}[v](i) = \sum_{j \in \Delta_i} w(i, j) * v(j). \tag{2}$$

The distance metric is proportional to the square of Euclidian distance between the two patches. The weight is then calculated as

$$w(i, j) = \frac{1}{Z_i} \exp\left\{ -\frac{||v(N_i) - v(N_j)||^2_{2,a}}{h^2} \right\}. \tag{3}$$

Based on (3), it is clear that the weight is the convolution of a Gaussian with standard deviation $a > 0$ and the squared Euclidean distance between two neighbourhoods $||v(N_i) - v(N_j)||_2^2$, for N_i and N_j. The smoothing parameter h controls the contribution of the Gaussian-Euclidean distance exponent in the weights. The normalization factor Z_i for pixel i is given by

$$Z(i) = \sum_{j \in \Delta_i} \exp\left\{ -\frac{||v(N_i) - v(N_j)||_{2,a}^2}{h^2} \right\}, \tag{4}$$

where the weight is normalized to ensure that the dynamic range of the NLM$[v](i)$ is the same as that of its counterpart $v(i)$.

2.4.2 The proposed Bayesian CODE framework

Noise in ultrasound B-mode images originates from piezoelectric sensors and data acquisition card. Depending on the application, the level of noise can even be higher. For example, ablation treatment generates heat and micro-bubbles that severely deteriorate RF data Jiang et al. (2009); Rivaz et al. (2008); Varghese et al. (2003). Both logarithmic compression and envelope detection steps, applied to derive the B-mode image, are non-linear operations that complicate measurement noise added by sensors and acquisition card. Our CODE approach eliminates noise introduced by sensors and acquisition card before the non-linear logarithmic compression and envelope detection by applying NLM directly to RF ultrasound data.

I now provide an analytical explanation of why NLM denoising is adapted for the RF domain. Let **g(x)** and **o(x)** be vectorized ground truth and observed patches of size n centered at pixel x_i of RF data (Figure 3.2). I define them as **g(x)** $:= g(x_k)$ with $x_k \in N_g(x)$ and **o(x)** $:= o(x_k)$, where $x_k \in N_o(x)$ and $\{N_o, N_g\}$ are the neighbourhoods (patches) of size $(\sqrt{n} \times \sqrt{n})$ around the central pixel x in ground truth and observed images. Our goal is to derive the Bayesian estimator **ĝ(x)** for patch **g(x)** based on the observed patch **o(x)**. Defining the optimal estimator by minimizing the posterior expected loss as

$$\mathbb{E}[L(\mathbf{g(x)}, \hat{\mathbf{g}}\mathbf{(x)})] = \sum_{\mathbf{g(x)} \in \Gamma} [L(\mathbf{g(x)}, \hat{\mathbf{g}}\mathbf{(x)})] p(\mathbf{g(x)}|\mathbf{o(x)}), \tag{5}$$

where Γ constitutes all possible outcomes of $\mathbf{g(x)}$, the loss function is given by

$$L(\mathbf{g(x)}, \hat{\mathbf{g}}(\mathbf{x})) = \|\mathbf{g(x)} - \hat{\mathbf{g}}(\mathbf{x})\|^2 . \tag{6}$$

Substituting (6) in (5), the optimal Bayesian estimator is

$$\begin{aligned} \hat{\mathbf{g}}(\mathbf{x})_{opt} &= \arg\min_{\hat{\mathbf{g}}(\mathbf{x})} \sum_{\mathbf{g}(x)} \|\mathbf{g(x)} - \hat{\mathbf{g}}(\mathbf{x})\|^2 p(\mathbf{g(x)}|\mathbf{o(x)}) \\ &= \sum_{\mathbf{g(x)}} \mathbf{g(x)} p(\mathbf{g(x)}|\mathbf{o(x)}). \end{aligned} \tag{7}$$

Equation (7) can be expressed as

$$\hat{\mathbf{g}}(\mathbf{x})_{opt} = \sum_{\mathbf{g(x)}} \mathbf{g(x)} \frac{p(\mathbf{g(x)}, \mathbf{o(x)})}{p(\mathbf{o(x)})} = \frac{\sum_{\mathbf{g(x)}} \mathbf{g(x)} p(\mathbf{o(x)}|\mathbf{g(x)}) p(\mathbf{g(x)})}{\sum_{\mathbf{g(x)}} p(\mathbf{o(x)}|\mathbf{g(x)}) p(\mathbf{g(x)})}. \tag{8}$$

Only a subset of Γ is accessible in the search region of central pixel x_i. I refer to this subset as the search region, $\text{SR}(\mathbf{x})) = \{\mathbf{g}_1(x), \mathbf{g}_2(x), \mathbf{g}_3(x), ..., \mathbf{g}_K(x)\}$. Assuming that cardinality of SR is K, and $p(\mathbf{g(x)})$ is uniformly distributed, i.e., $p(\mathbf{g}_i(x)) = 1/n$. Equation (8) simplifies to

$$\hat{\mathbf{g}}(\mathbf{x}) = \frac{\sum_{j=1}^{K} \mathbf{g}(x_j) p(\mathbf{o}(x_i)|\mathbf{g}(x_j))}{\sum_{j=1}^{K} p(\mathbf{o}(x_i)|\mathbf{g}(x_j))}, \tag{9}$$

where $\hat{\mathbf{g}}(\mathbf{x})$ is the optimal estimator based on the uniform distribution assumption. Given the ground truth is not accessible, I substitute the observed value of the neighbourhood patches to get

$$\hat{\mathbf{g}}(\mathbf{x}) = \frac{\sum_{j=1}^{K} \mathbf{o}(x_j) p(\mathbf{o}(x_i)|\mathbf{o}(x_j))}{\sum_{j=1}^{K} p(\mathbf{o}(x_i)|\mathbf{o}(x_j))}. \tag{10}$$

Given that the noise in the RF data is modelled as an additive Gaussian noise Teixeira et al. (2017); Viola and Walker (2003), I have

$$\mathbf{o(x)} = \mathbf{g(x)} + \mathbf{v(x)}, \tag{11}$$

where $\mathbf{v(x)}$ is the additive white Gaussian noise with variance σ^2. By assuming that the likelihood

can be factorized as

$$p(\mathbf{o}(x_i)|\mathbf{o}(x_j)) = \prod_{k=1}^{n} p(o(x_{i,k})|o(x_{j,k})), \tag{12}$$

where $x_{i,k} \in N(x_i)$ and $x_{j,k} \in N(x_j)$ are the counterpart pixels in the patches with central pixels x_i and x_j. Therefore, $p(\mathbf{o}(x_i)|\mathbf{o}(x_j))$ is multivariate normal distributed $p(\mathbf{o}(x_i)|\mathbf{o}(x_j)) \sim \mathcal{N}(\mathbf{o}(x_j), \sigma^2 I_n)$. Notation I_n is the identity matrix. Thus, the filter in (10) can be adapted to remove the noise of RF data as

$$\begin{aligned} \hat{\mathbf{g}}(\mathbf{x}) &= \frac{1}{C(x_i)} \sum_{j=1}^{K} \exp^{-\frac{\|\mathbf{o}(x_i)-\mathbf{o}(x_j)\|^2}{h^2}} \mathbf{o}(x_j), \\ \text{with} \qquad C(x_i) &= \sum_{j=1}^{K} \exp^{-\frac{\|\mathbf{o}(x_i)-\mathbf{o}(x_j)\|^2}{h^2}}. \end{aligned} \tag{13}$$

Equation (13) is also known as NLM algorithm. By considering the normal distributed assumption, equation (13) can be adapted for denoising the RF data by replacing $h^2 = 2\sigma^2$. Therefore, the adapted filter for denoising the RF data (CODE) is

$$\begin{aligned} \hat{\mathbf{g}}(\mathbf{x}) &= \frac{1}{C(x_i)} \sum_{j=1}^{K} \exp^{-\frac{\|\mathbf{o}(x_i)-\mathbf{o}(x_j)\|^2}{2\sigma^2}} \mathbf{o}(x_j), \\ \text{with} \qquad C(x_i) &= \sum_{j=1}^{K} \exp^{-\frac{\|\mathbf{o}(x_i)-\mathbf{o}(x_j)\|^2}{2\sigma^2}}. \end{aligned} \tag{14}$$

This filter is based on the noise statistics of RF data. CODE is, therefore, the optimal denoising approach for removing noise in model (11) within the RF domain.

Kevrann et al. Kervrann et al. (2007) and Coupe et al. Coupé et al. (2009) have developed similar Bayesian estimators but for reducing the speckles pattern in the B-mode image. Aligned with the mathematical Bayesian estimator, the properties of noise in RF data show the usefulness of CODE for removing noise from the RF ultrasound data.

Table 2.1: Values of Chi squared and SSD for reconstructed images. The ground truth was obtained from a Field II simulation.

Scatterers	Chi^2			SSD		
	NLM	Gaussian	CODE	NLM	Gaussian	CODE
$5/mm^3$	9702.33	167.78	**95.49**	76250.03	2240.55	**2119.90**
$10/mm^3$	86361.68	253.65	**60.18**	7482.55	2242.51	**1909.44**
$15/mm^3$	6108.31	294.90	**27.63**	7961.00	2300.42	**1536.20**

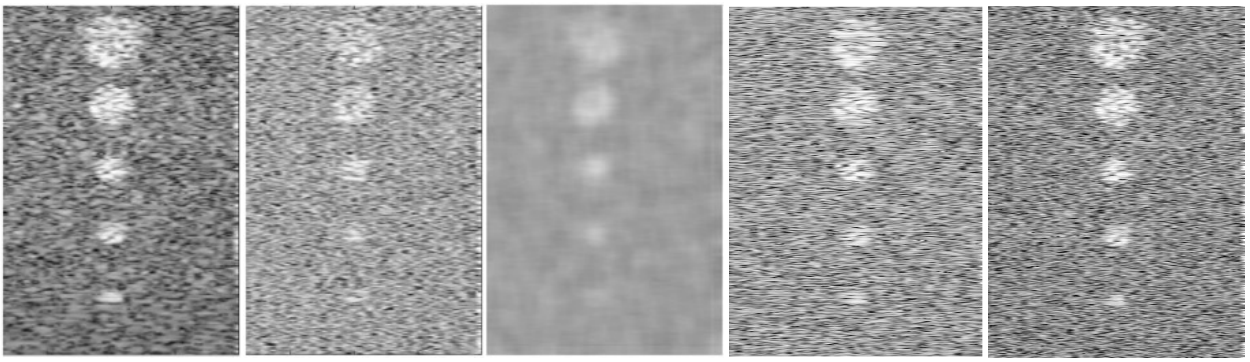

(a) Ground-truth (b) Noisy (c) NLM (d) Gaussian on RF (e) CODE

Figure 2.3: Field II simulation results. The noisy input has substantially less contrast than the ground-truth image. NLM is designed to remove speckle and therefore substantially reduces image detail. CODE output is closest to the ground-truth.

2.5 Validation of Code Using Simulation Experiments

To assess the performance of CODE approach, the Field II Jensen (1996) software is used to simulate RF data from a lesion phantom of size 60, 50 and 10mm in axial, lateral and out-of-plane directions respectively. The size of RF is $1476 * 50$. The phantoms consist of two classes of background and target tissues. To determine the precision and sensitivity of the CODE, three different setups with 5, 10, and 15 scatterers per resolution cell distributed randomly within the phantom are used. Different realizations for each group of scatterers are generated. The RF output of Field II is corrupted by adding additive white Gaussian noise with a SNR of 5dB.

Figure 2.3 shows the results of NLM applied to B-mode images. As expected, NLM performs incoherent averaging and removes speckle pattern. This is desired for many applications such as segmentation and registration Zhou and Rivaz (2016), but not in elastography. Figure 2.3 also

shows the results of applying a Gaussian kernel to the RF data. Since averaging is performed in the RF domain, the speckle pattern is retained. Finally, the results of CODE denoising is also shown in this figure, which visually outperforms other methods in terms of similarity to the original B-mode image. Figure 2.4 compares the histogram of the B-mode of these three images. Since the distribution of noise-free image (ground truth) is known, I used the following chi-square test as a quantitative parameter for comparison

$$\chi^2 = \sum_{t=1}^{m} \frac{(O_t - E_t)^2}{E_t}, \tag{15}$$

where O_t is the observed value, E_t the expected value and m number of bins (256 bins of grey levels for simulated images). The Chi squared criterion for distribution and sum of squared difference (SSD) between original and filtered images using NLM, Gaussian with kernel width of 5 and smoothing parameter 1, and CODE with search region 21, kernel width 5 and smoothing parameter 5, are compared in Table 2.1. In both cases (Chi squared and SSD), CODE outperforms the conventional NLM approach and Gaussian denoising applied directly on RF data, as demonstrated in theory in Section 2.4.2.

Moreover, with respect to simulations in Field II, the ground truth is available to study error variance of all 3 distributions of scatterers. The error variance is measured using Normalized Root Mean Square Error (NRMSE), defined as

$$NRMSE(G, I_d) = \frac{\sqrt{\frac{\sum_{i=1}^{n}\sum_{j=1}^{m}(I_d(i,j)-G(i,j))^2}{m*n}}}{Max(G) - Min(G)}, \tag{16}$$

where G is ground truth of Field II, I_d is either noisy image or denoised version using NLM or Gaussian denoising. Table 2.2 shows the error variance for the CODE method is minimum in compare with other denoising.

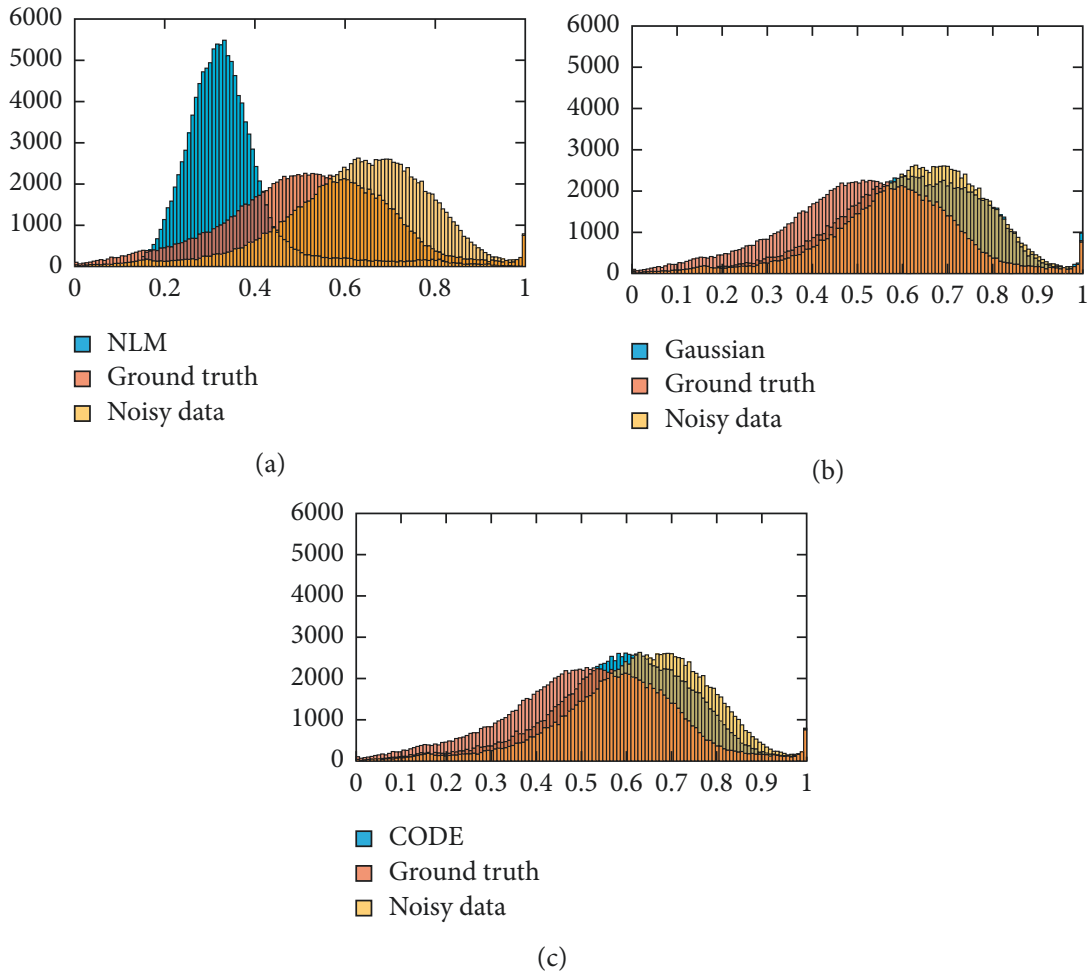

Figure 2.4: (a) Histograms of NLM, ground truth, and noisy data. (b) Histograms of Gaussian denoising, ground truth, and noisy data. Finally, (c) is the same as (b) except the histogram of NLM replaced by that of CODE.

Table 2.2: using Filed II ground truth for evaluation of NRMSE for different denoising and noisy image.

Method	5/mm^3	10/mm^3	15/mm^3
Noisy	0.1501	0.1298	0.1284
NLM	0.3210	0.3208	0.3182
Gaussian	0.1595	0.1478	0.1442
CODE	**0.1354**	**0.1216**	**0.1203**

2.6 Phantom and *In-vivo* Elastography

I study 3 different cases of phantom data, *in-vivo* liver ablation data and tendon data for both GLUE and DPAM. The results are provided in Figs. 2.5-2.10. The window size of 3 provide correct strain map, for CODE meanwhile requires the minimum computational budget. To be fair in comparison, the window size is the same for both NLM and Gaussian denoising.

Phantom data in Figure 2.7 and Figure 2.6 is obtained from a CIRS breast phantom (Norfolk, VA) under freehand palpation. There is excessive out of plane motion between the two processed images, and therefore, the DP step fails. This leads to failure in both DPAM and GLUE, which is apparent as black horizontal artifacts in (a), (c) and black artifact at right down corner of (d) for both mentioned Figures. However, CODE removes the noise from the RF data and leads to a strain image with low noise and high contrast. The phantom contains a cyst in the middle with certain elasticity surrounded by another tissue. Those artifacts as describe, are failing to depict the tissue around the cyst or the cyst elasticity by showing different elasticities.

Patient data in Figure 2.7 and Figure 2.8 was acquired from a patient undergoing open surgical radio-frequency thermal ablation for primary or secondary liver cancer. This data is available online Rivaz et al. (2011). The Institutional Ethical Review Board at Johns Hopkins University approved all experimental procedures involving human subjects. For the patient data, ablation procedure generates substantial amount of noise in the RF data Jiang et al. (2009); Rivaz et al. (2008); Varghese et al. (2003). As a result of excessive noise, DP fails, which generates the horizontal black and white band in the top left of (a), (c) and (d). Although the environment is extremely noisy, the well-adapted CODE method denoises the RF data in a way that both algorithms are able to get the correct strain map for patient data. The ablation operation coagulates the tissue, which makes the

tissue stiffer. The coagulated tissue is often referred to as ablation lesion, and its size should be bigger than the tumor to ensure that the entire tumor is ablated. The strain images in Figure 2.7.(b) and Figure 2.8.(b) clearly show the ablation lesion as a dark region with low strain (i.e. hard). CODE helps remove noise in RF data, which leads to less noisy strain images. Such strain images can help the surgeon to minimize the cancer recurrence rate. However, NLM and Gaussian fail to reconstruct the strain map and show sudden changes in tissue that are misleading and violate tissue continuity.

I also evaluate CODE on data collected from patellar tendon. This data was collected at the PERFORM Centre at Concordia University. Ethics approval was obtained for this study from Quebec's Ministere de la Sante et des Services Sociaux and all subjects signed a consent form to participate. Data is collected using an Alpinion E-Cube ultrasound machine (Bothell, WA) with a L3-12 linear transducer and at the center frequency of 11MHz with sampling frequency of 40MHz. The results are shown in Figure 2.9 and Figure 2.10. The probe is held stationary, and the subject flexes his knee joint during data collection. CODE removes the noise in the RF data and results in a more meaningful strain image. Some of the data used in this chapter are available online Rivaz et al. (2011).

2.7 Conclusions

In this chapter, I have proposed a denoising algorithm, referred to as the CODE (COherent Denoising for Elastography) approach for ultrasound elastography. CODE is applied directly to the RF data, and has the ability to eliminate noise, while retaining relevant speckle patterns. This is demonstrated using phantom and experiments based on *in-vivo* clinical data. The results of CODE are used for GLUE and DPAM, which verifies the effectiveness of the proposed CODE. More clinical studies are needed to fully verify the benefits of the CODE algorithm.

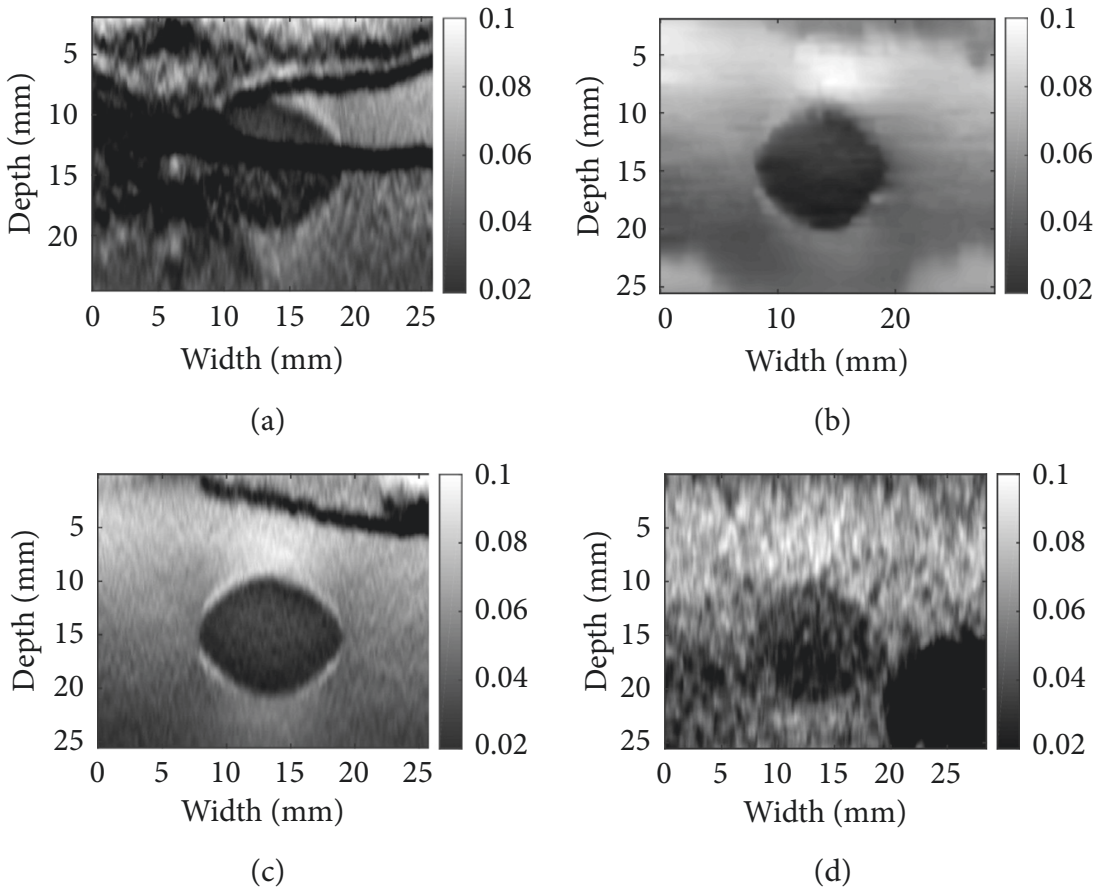

Figure 2.5: Denoising results for phantom data: (a) DPAM alone; (b) DPAM with CODE; (c) DPAM with Gaussian (d) DPAM with NLM. For CODE, the dimensions of the search window is (11×11), size of the neighbourhood is (3×3), and the smoothing parameter h is set to 11. For (c), the kernel size is (3×3) and smoothing parameter is 1. For (d), the NLM properties is set as (b) but it is applied on B-mode.

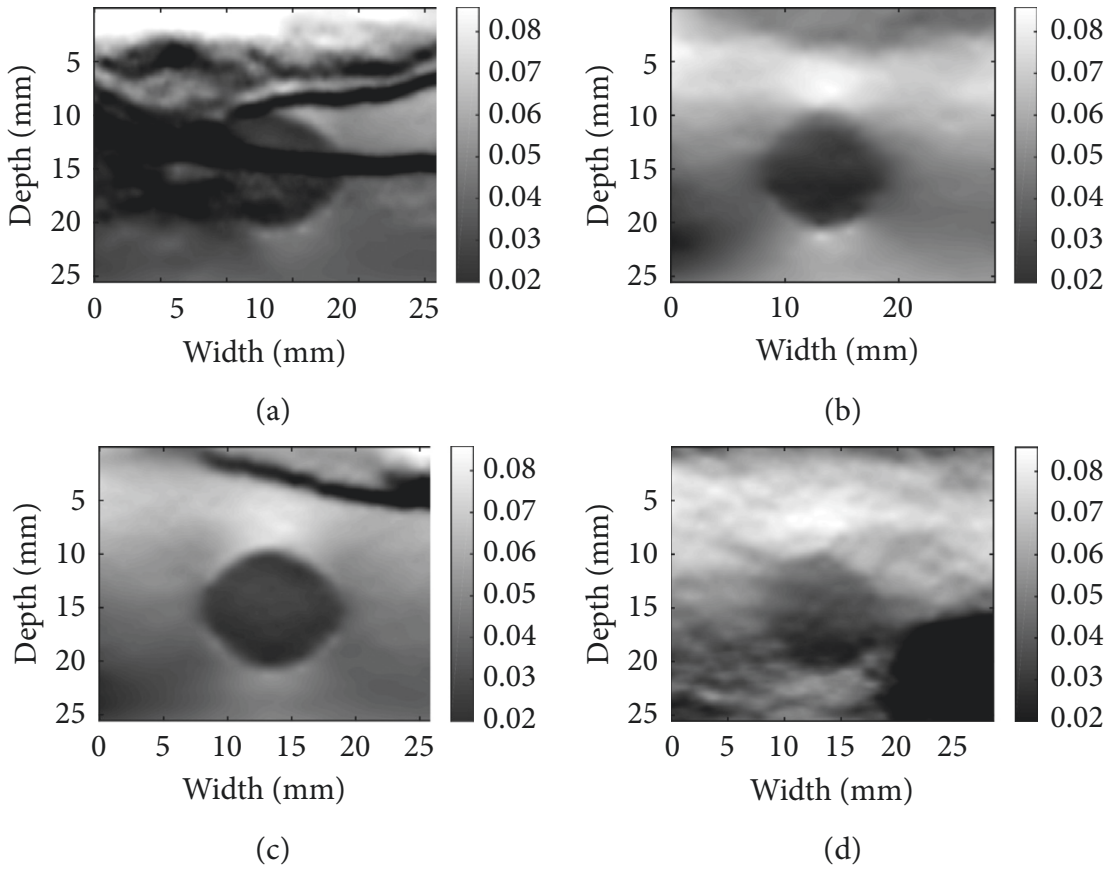

Figure 2.6: Denoising results for phantom data: (a) GLUE alone; (b) GLUE with CODE; (c) GLUE with Gaussian (d) GLUE with NLM. For CODE, the dimensions of the search window is (11×11), size of the neighbourhood is (3×3), and the smoothing parameter h is set to 11. For (c), the kernel size is (3×3) and smoothing parameter is 1. For (d), the NLM properties is set as (b) but it is applied on B-mode.

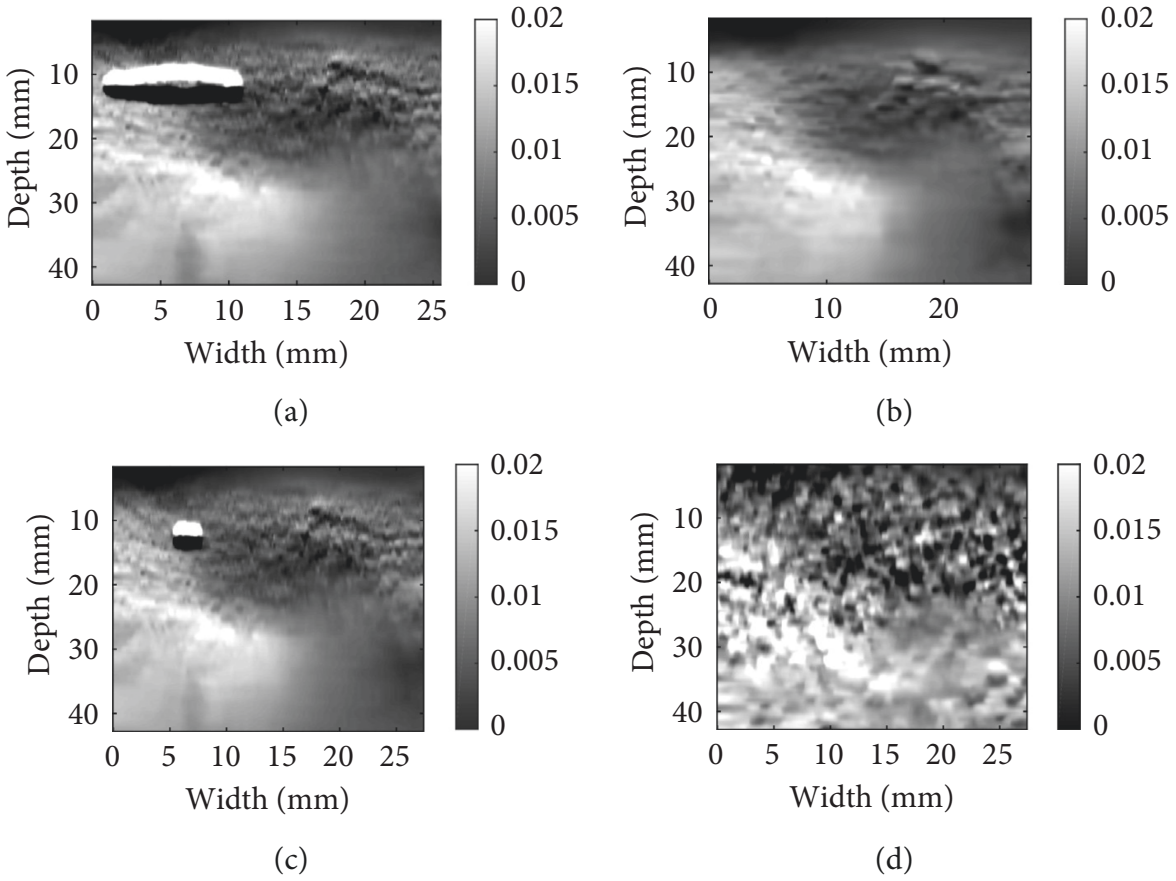

Figure 2.7: Same as Fig. 2.5 except in-vivo liver ablation patient data is used: (a) DPAM alone; (b) DPAM with CODE; (c) DPAM with Gaussian (d) DPAM with NLM.

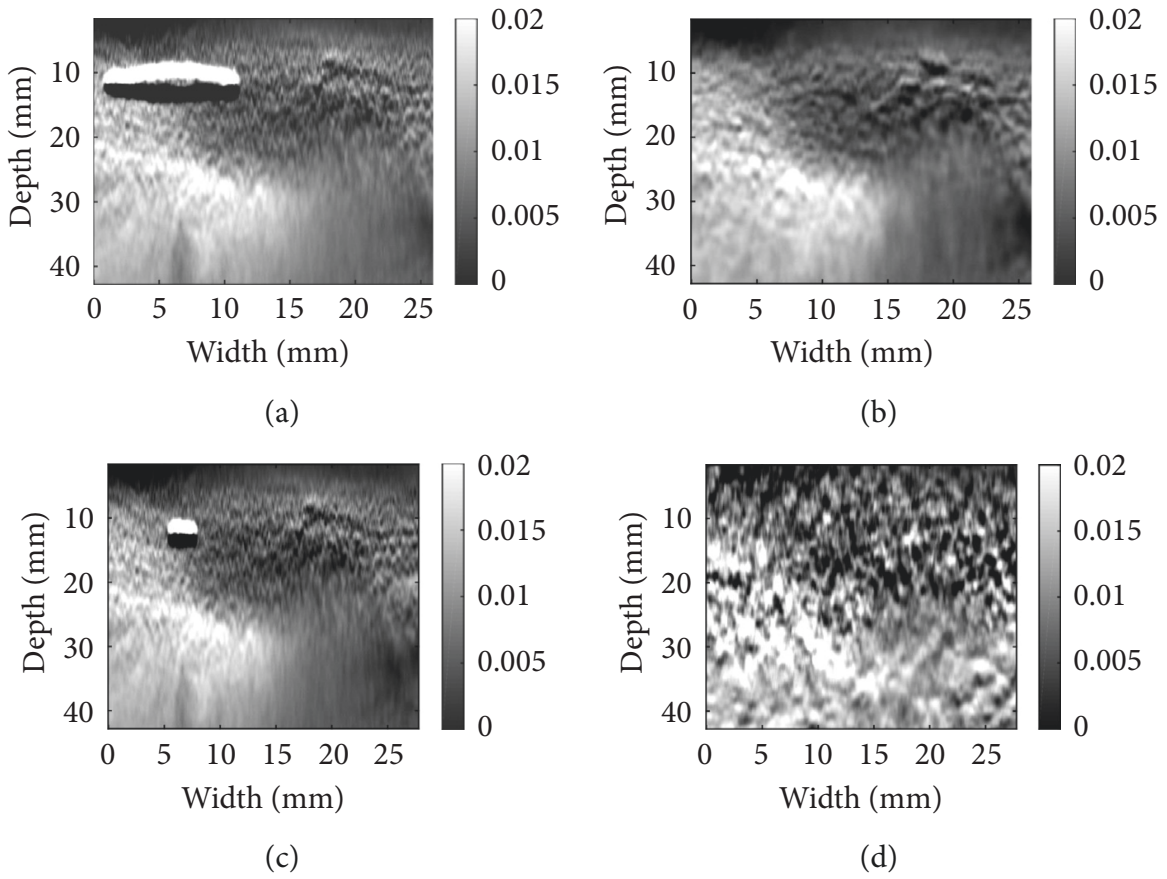

Figure 2.8: Same as Fig. 2.6 except in-vivo liver ablation patient data is used: (a) GLUE alone; (b) GLUE with CODE; (c) DPAM alone; (d) DPAM with CODE.

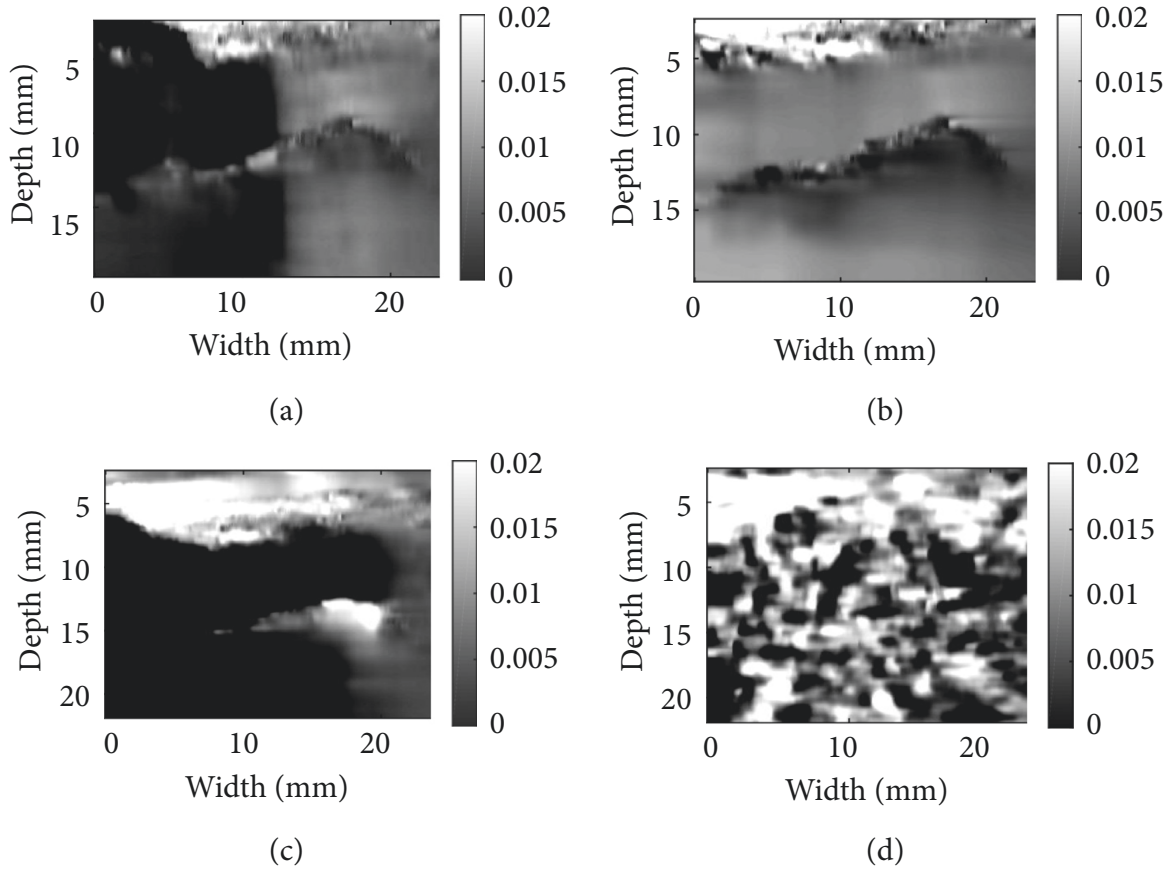

Figure 2.9: Same as Fig. 2.5 except in-vivo patient tendon data is used: (a) DPAM alone; (b) DPAM with CODE; (c) DPAM with Gaussian; (d) DPAM with NLM.

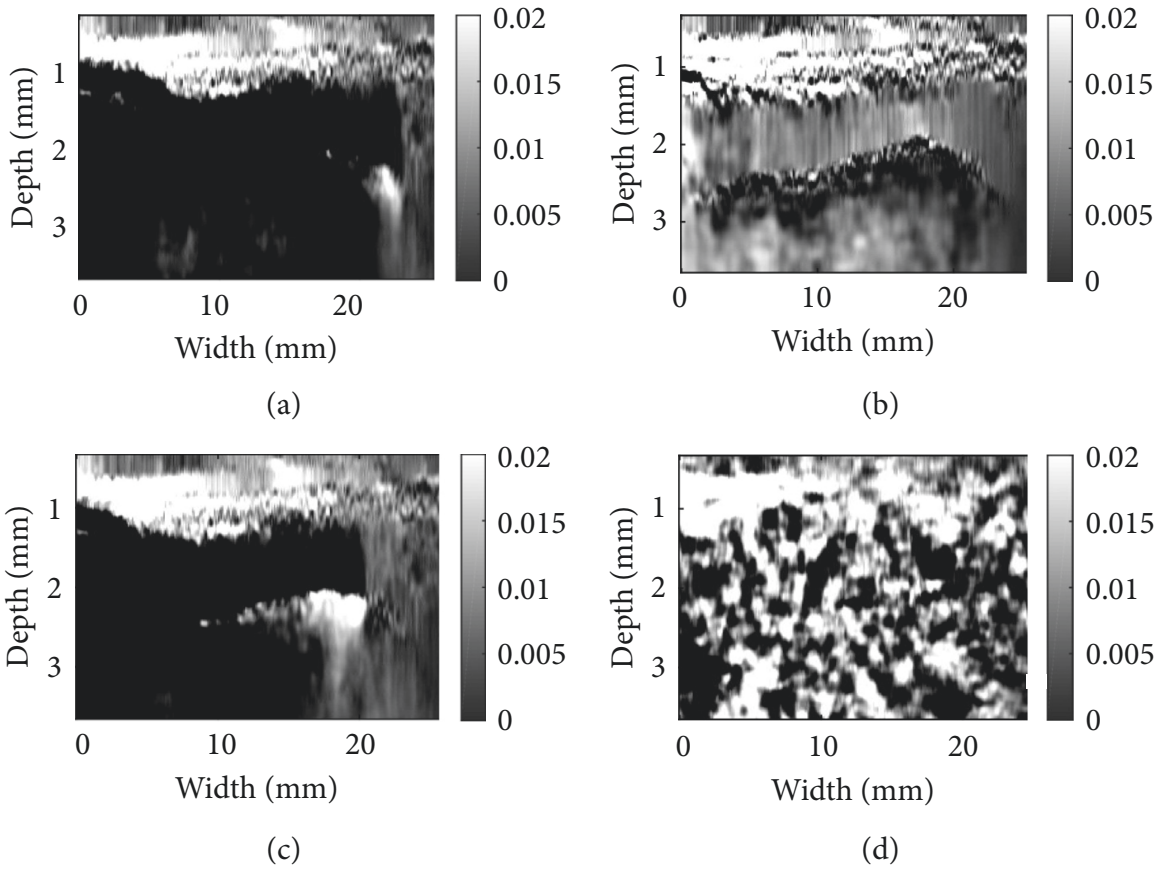

Figure 2.10: Same as Fig. 2.6 except in-vivo patient tendon data is used: (a) GLUE alone; (b) GLUE with CODE; (c) GLUE with Gaussian; (d) GLUE with NLM.

Chapter 3

Coherent Super Resolution in Ultrasound

3.1 Overview

The resolution of ultrasound (US) images is limited by physical constraints and hardware restrictions, such as the frequency, width and focal zone of the US beam. Different interpolation methods are often used to increase the sampling rate of ultrasound images. However, interpolation methods generally introduce blur in images. Herein, I present a super resolution (SR) algorithm for reconstruction of the B-mode images using the information from the envelope of radio frequency (RF) data. Our method is based on utilizing repetitive data in the non-local neighborhood of samples. The performance of the proposed approach is determined both qualitatively and quantitatively using phantom and *in-vivo* data.

3.2 Introduction

Ultrasound is a commonly used medical imaging modality since it is non-invasive, real-time, portable, and inexpensive. However, US images are intrinsically noisy and, therefore, numerous methods are used to increase the quality of the data. These procedures are applied to improve the quality of ultrasound (US) images, or, as a preprocessing step to perform high-level image analysis

tasks Coupé et al. (2009); Montaldo et al. (2009); Ramos-Llordén et al. (2015). Extensive previous work exists on the enhancement of US images and on the impact it has on image analysis techniques, such as image segmentation Cunningham et al. (2017); Stevenson et al. (2015) and registration Rivaz et al. (2015); Shams et al. (2018). Various interpolation approaches have been proposed to increase the number of samples in US images Housden et al. (2006); Kortbek et al. (2005).

Several factors such as physical hardware, limitation on the processing time, and poor signal to noise ratio limit the quality of the images in medical imaging modalities such as US. Interpolation techniques are therefore applied in the aforementioned scenarios to improve the quality of the images Lehmann et al. (1999); Thévenaz et al. (2000).

Interpolation methods assume that high resolution (HR) patches can be represented by a polynomial function under some smoothing assumptions. However, in US imaging, the pattern of B-mode images is very variable and may invalidate these assumptions. An alternative approach to improve the resolution in the B-mode images of US is based on the super resolution (SR) techniques. In the SR process, one or more HR patches are reconstructed based on corresponding one or more low resolution (LR) observations Ledig et al. (2016); Nasrollahi and Moeslund (2014). Multi image SR techniques try to restore the HR images based on samples of LR patches in the temporal domain Protter et al. (2009), or using machine learning techniques Dong et al. (2016). Nevertheless, due to scarcity of ground truth and training data sets in the US images, I choose the single image SR path. In the single image SR, which can be classified as interpolation- and recursion-based, the process often attempts to recreate the HR images from information in LR observations of a single image.

In this chapter, I propose a recursive image reconstruction on the envelope of US images that preserves delicate structure while maintaining the margin between different issues. The rest of the chapter is organized as follows. In Section 3.3, I explore the proposed method in detail and provide a mathematical framework that validates the proposed approach as a Bayesian estimation. In Section 3.4, I evaluate the performance of the proposed method using different measures on both *in-vivo* and phantom data, and I conclude the chapter in Section 3.5. This chapter has been accepted as a paper to Multimedia Signal Processing Conference (MMSP 2018), but has not been published yet.

3.3 Super Resolution

In US imaging, interpolations for upsampling the US images are based on an assumption that HR pixels can be expressed in terms of LR pixels. To simplify our explanation, I focus on 1D signals but our results are generalizable to 2D images. Mathematically speaking, let y_n be a LR noisy pixel in the image. Assume pixels in the HR image are denoted as x_i, then y_n can be expressed as:

$$y_n = \frac{1}{N} \sum_{i=1}^{N} x_i + n, \tag{17}$$

where in RF data, n can be consider as Gaussian noise and N is the size of the averaging filter. Within *neighborhoods* of LR pixels, the interpolation algorithm can be used to reconstruct the HR pixels by assigning the weights to them as follows:

$$x_i = \begin{cases} \sum_{j \in \Omega} w_{ij} y_j & \text{if } i \neq j \\ y_j & \text{if } i = j \end{cases} \tag{18}$$

where symbol Ω is a neighborhood of pixels in the HR image. The weights, ω_{ij}, are calculated as a function based on the distance between the location of HR pixel and LR ones. If the location of the pixels are the same, the value of LR pixel y_j is kept for HR pixel x_i.

The goal of SR or interpolation algorithms is to find values for x_i using the eq. (17). This problem is an ill-posed problem because there are infinite values for x_i that satisfy eq. (17). In the next section, a new algorithm is proposed for upsampling the US images using information in a *non-local neighborhood* of pixels.

3.3.1 Non-local Super Resolution Approach

The proposed method (illustrated by the block diagram in Figure 3.1) is based on denoising the noisy data first and then applying the SR method on the denoised data. The input RF data is denoised using the non-local means (NLM) based approach on RF data. The output of the denoising

filter will be y that is the denoised version of y_n.

$$y = \frac{1}{N}\sum_{i=1}^{N} x_i. \tag{19}$$

The eq. (19) can be rewritten as

$$y - \frac{1}{N}\sum_{i=1}^{N} x_i = 0. \tag{20}$$

This equation enforces the upscaled image to be consistent and is referred to as the *subsampling consistency* Banerjee and Jawahar (2008). I used this equation as the stopping criterion for the SR algorithm.

In the next step, an iterative process is exploited to extract the information of LR patches. It consists of two separate blocks, used to: (i) smooth the image without losing edges (non-local means), and (ii) update the HR part from the LR denoised pixels. The input to the algorithm is the preprocessed LR image y and the stopping criterion sc for the algorithm. sc is set to 0.01% for err function output value and algorithm halts in cases when the err function returns a value less than sc. The err function gives the average of absolute value difference between its arguments 21.

$$err(a, b) = 1/N \sum_{n=1}^{N} abs(a - b). \tag{21}$$

The upsampling and downsampling operations are used in the SR algorithm for making the number of computations and comparisons equal. Firstly, y is upsampled to the desire aspect ratio and dimensions. In our case, the upscaling factor is set to 2 and has been done using bicubic interpolation. Assuming that x' is the approximation output of x and considering the interpolation operation as U, the output will be

$$x' = U(y). \tag{22}$$

The other blocks of this figure (fig. 3.1) are elaborated in the next subsections. I investigate the NLM algorithm for assuring smoothing in the neighborhood of pixel and then by using the subsampling consistency of eq. (20). The error of difference between y and downsampled version of x' is used to refine the algorithm output x'.

Patch-wise Smoothing

Let $x'(i)$ be the observed value of the discretized image for pixel i and $x(i)$ be its true value. Due to the presence of noise $n(i)$, I have

$$x'(i) = x(i) + n(i). \tag{23}$$

To remove the distortion present in image for each pixel i, NLM searches a reference area of the image within a rectangular *search window* Ω_i, which is centered around pixel i. A neighborhood N_i of known dimensions is selected around pixel i and compared to neighborhood N_j around pixel j for all $j \in \Omega_i$. For pixel i, weight $w(i,j)$ is assigned to each pixel j. The value of pixel i is then replaced by

$$\text{NLM}[x'](i) = \sum_{j \in \Omega_i} w(i,j) * x'(j). \tag{24}$$

The distance metric is proportional to the square of Euclidean distance between the two patches. The weight is then calculated as

$$w(i,j) = \frac{1}{Z_i} \exp\left\{ -\frac{||x'(N_i) - x'(N_j)||^2_{2,a}}{h^2} \right\}. \tag{25}$$

Based on (25), it is clear that the weight is the convolution of a Gaussian with standard deviation $a > 0$ and the squared Euclidean distance between two neighborhoods $||x'(N_i) - x'(N_j)||^2_2$, for N_i and N_j. The smoothing parameter h controls the contribution of the Gaussian-Euclidean distance exponent in the weights. The normalization factor Z_i for pixel i is given by

$$Z(i) = \sum_{j \in \Delta_i} \exp\left\{ -\frac{||x'(N_i) - x'(N_j)||^2_{2,a}}{h^2} \right\}, \tag{26}$$

where the weight is normalized to ensure that the dynamic range of the NLM$[x'](i)$ is the same as that of its counterpart $x'(i)$. The NLM is applied to the envelope of RF data. More details of the NLM implementation are presented in Section 3.3.2.

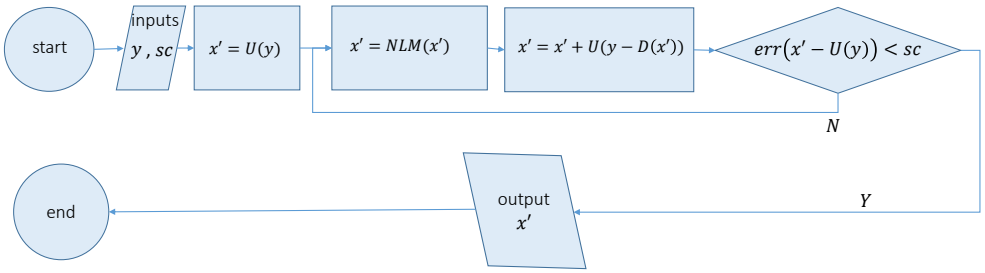

Figure 3.1: The flowchart for the proposed method. The inputs are the LR patch and stopping criterion (y and sc), and the output is x' that is the HR patch. The operator U stands for upsampling using bicubic interpolation. The err function returns the mean of absolute value difference between its arguments.

Retrieving Low Resolution Pixels

The LR pixels, y, are observations that are assumed to be the ground truth for reconstruction of the HR image. For retrieving the pixels in the LR patch, the algorithm upsamples the difference between LR patch and corresponding pixels in the upsampled image, x' using a downsampling operation. This difference is upsampled using interpolation and added to the existing x' to create the updated x':

$$x' = x' + U(y - D(x')), \tag{27}$$

where D and U are downsampling and upsampling operations, respectively. Finally, the error is evaluated based on the upsampled image x' and upsampled version of the LR patch y. If the stopping criterion is met, the algorithm halts. Fig. 3.1 shows the flowchart of the proposed algorithm. Similar to Coupe et al. Coupé et al. (2009) and Kevrann et al. Kervrann et al. (2007), next I suggest a Bayesian framework that provides the mathematical foundation of the proposed algorithm.

3.3.2 Bayesian Framework

This framework is similar to the framework that I have followed in the Chapter 2. Suppose **g(x)** and **o(x)** are vectorized ground truth and upscale of observed version patches of size n centered at x of the radio frequency data, defined as **g(x)** $:= g(x_k)$ and $x_k \in N_g(x)$ and **o(x)** $:= o(x_k)$, where $x_k \in N_o(x)$ (N_o and N_g are the neighborhoods (patch) of size $\sqrt{n}$ by $\sqrt{n}$ around the central pixel x in the ground truth and observed images.) The goal is to get the Bayesian estimator, $\hat{\mathbf{g}}$**(x)**, of patch

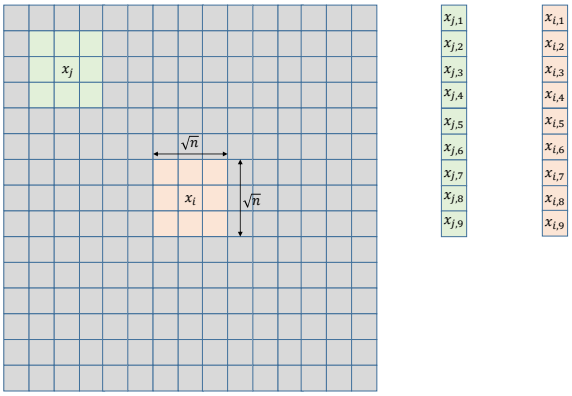

Figure 3.2: An example of illustration patches of an observed radio frequency image. Patches and corresponding vectorized indices are presented in this figure for $n = 9$.

g(x) based on the observed patch **o(x)**. Let's define optimal estimator by minimizing the posterior expected loss as follows

$$E[L(\mathbf{g(x)}, \hat{\mathbf{g}}(\mathbf{x}))] = \sum_{\mathbf{g(x)} \in \Gamma} [L(\mathbf{g(x)}, \hat{\mathbf{g}}(\mathbf{x}))] p(\mathbf{g(x)}|\mathbf{o(x)}), \tag{28}$$

where Γ is all possible configurations of **g(x)**. The loss function is defined as

$$L(\mathbf{g(x)},\hat{\mathbf{g}}(\mathbf{x})) = \|\mathbf{g(x)} - \hat{\mathbf{g}}(\mathbf{x})\|^2 . \tag{29}$$

If eq. (29) is substituted in eq. (28), the optimal Bayesian estimator, $\hat{\mathbf{g}}(\mathbf{x})_{opt}$, is given by

$$\begin{aligned} \hat{\mathbf{g}}(\mathbf{x})_{opt} &= arg \min_{\hat{\mathbf{g}}(\mathbf{x})} \sum_{\mathbf{g}(x)} \|\mathbf{g(x)} - \hat{\mathbf{g}}(\mathbf{x})\|^2 p(\mathbf{g(x)}|\mathbf{o(x)}) \\ &= \sum_{\mathbf{g(x)}} \mathbf{g(x)} p(\mathbf{g(x)}|\mathbf{o(x)}). \end{aligned} \tag{30}$$

Then eq. (30) can be expressed as

$$\hat{\mathbf{g}}(\mathbf{x})_{opt} = \sum_{\mathbf{g(x)}} \mathbf{g(x)} \frac{p(\mathbf{g(x)}, \mathbf{o(x)})}{p(\mathbf{o(x)})} = \frac{\sum_{\mathbf{g(x)}} \mathbf{g(x)} p(\mathbf{o(x)}|\mathbf{g(x)}) p(\mathbf{g(x)})}{\sum_{\mathbf{g(x)}} p(\mathbf{o(x)}|\mathbf{g(x)}) p(\mathbf{g(x)})}. \tag{31}$$

Note that only a subset of Γ is accessible in the search region of central pixel x_i. I refer to this subset as the search region, $SR(\mathbf{x})) = \{\mathbf{g}_1(x), \mathbf{g}_2(x), \mathbf{g}_3(x), ..., \mathbf{g}_K(x)\}$. Assuming that K is number of samples in the SR (the number of members in, I get the mentioned subset) and $p(\mathbf{g(x)})$ is uniformly distributed

$$p(\mathbf{g}_i(x)) = \frac{1}{n}. \tag{32}$$

Based on these assumptions, eq. (31) leads to

$$\begin{aligned} \hat{\mathbf{g}}(\mathbf{x}) &= \frac{\frac{1}{K}\sum_{j=1}^{K} \mathbf{g}(x_j) p(\mathbf{o}(x_i)|\mathbf{g}(x_j))}{\frac{1}{K}\sum_{j=1}^{K} p(\mathbf{o}(x_i)|\mathbf{g}(x_j))} \\ &= \frac{\sum_{j=1}^{K} \mathbf{g}(x_j) p(\mathbf{o}(x_i)|\mathbf{g}(x_j))}{\sum_{j=1}^{K} p(\mathbf{o}(x_i)|\mathbf{g}(x_j))}, \end{aligned} \tag{33}$$

where $\hat{\mathbf{g}}(\mathbf{x})$ is the optimal estimator based on assumption (32). However, there is only the upscaled of observed values and the ground truth is not accessible. Consequently, I substitute the observed values of the neighborhood patches to get.

$$\hat{\mathbf{g}}(\mathbf{x}) = \frac{\sum_{j=1}^{K} \mathbf{o}(x_j) p(\mathbf{o}(x_i)|\mathbf{o}(x_j))}{\sum_{j=1}^{K} p(\mathbf{o}(x_i)|\mathbf{o}(x_j))}. \tag{34}$$

By assuming that the likelihood can be considered as (see Fig. 3.2)

$$p(\mathbf{o}(x_i)|\mathbf{o}(x_j)) \propto \exp^{-\|\mathbf{o}(x_i)-\mathbf{o}(x_j)\|^2}, \tag{35}$$

the estimator for $\hat{\mathbf{g}}(\mathbf{x})$ can be rewritten as

$$\begin{aligned} \hat{\mathbf{g}}(\mathbf{x}) &= \frac{1}{C(x_i)} \sum_{j=1}^{K} \exp^{-\|\mathbf{o}(x_i)-\mathbf{o}(x_j)\|^2} \mathbf{o}(x_j); \\ C(x_i) &= \sum_{j=1}^{K} \exp^{-\|\mathbf{o}(x_i)-\mathbf{o}(x_j)\|^2}. \end{aligned} \tag{36}$$

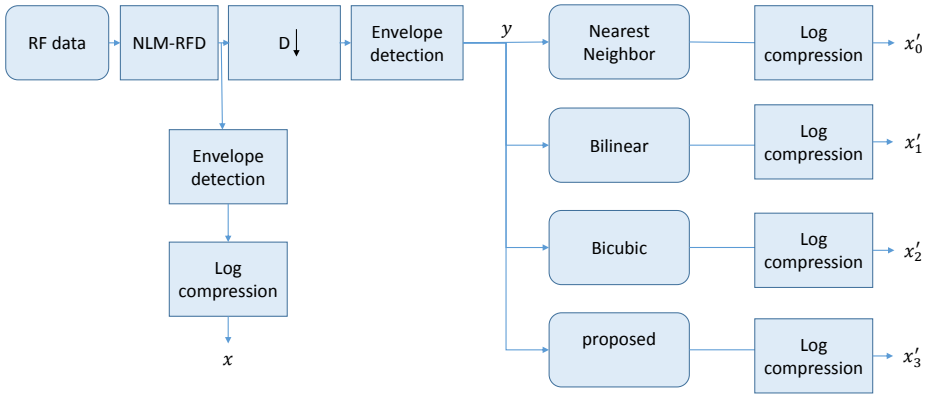

Figure 3.3: The flowchart for comparison of the proposed method.

For smoothing the similarities, the parameter h is introduced and final estimator for $\hat{\mathbf{g}}(\mathbf{x})$ is

$$\begin{aligned} \hat{\mathbf{g}}(\mathbf{x}) &= \frac{1}{C(x_i)} \sum_{j=1}^{K} \exp^{-\frac{\|\mathbf{o}(x_i)-\mathbf{o}(x_j)\|^2}{h^2}} \mathbf{o}(x_j); \\ C(x_i) &= \sum_{j=1}^{K} \exp^{-\frac{\|\mathbf{o}(x_i)-\mathbf{o}(x_j)\|^2}{h^2}}. \end{aligned} \tag{37}$$

The pixels of upsampled image can be grouped into two kinds of pixels, the synthesized pixels created by upsampling operation and the input pixels to upsampling algorithm. The Bayesian estimator can be used for the former group and the value of pixels in the latter group are retrieved from the output of SR algorithm as discussed in the algorithm illustrated in Fig. 3.1.

3.4 Experiments and results

In our experiments, phantom and *in-vivo* data have been studied. Phantom data in Fig 3.10 is obtained from a CIRS breast phantom (Norfolk, VA). Patients' data were acquired from patients undergoing open surgical radio frequency thermal ablation for primary or secondary liver cancer. The Institutional Ethical Review Board at Johns Hopkins University approved all experimental procedures involving human subjects. All data was collected using a Siemens Antares ultrasound machine (Issaquah, WA) with a VF10-5 linear probe.

Method	Patient 1	Patient 2	Patient 3	Phantom
NN	0.0538	0.1358	0.1232	0.1078
Bilinear	0.0472	0.1224	0.1085	0.0985
Bicubic	0.0461	0.1188	0.1057	0.0940
Proposed	**0.0225**	**0.0597**	**0.0544**	**0.0481**
decreased	**48.80%**	**50.25%**	**51.46%**	**51.70%**

Table 3.1: Sum of Absolute Differences (SAD) results of proposed method versus conventional interpolation methods

For the sake of comparison, three upsampling interpolations are used: the nearest neighbor interpolation, bilinear interpolation, and bicubic interpolation. First, I apply NLM for denoising the RF data and afterwards, by envelope detection and log compression, the HR image for comparison is constructed (as depicted in Fig. 3.3), called x of size R^{n*m}. The denoised RF data is then fed to a downsampler followed by an envelope detector to construct the LR image, y. I used the downsampling with a factor of 2. The LR image is upsampled using different interpolations and proposed method and after logarithmic compression the outputs are used for comparison, or equivalently x'_0 to x'_3 of size R^{n*m}. The parameters values for proposed algorithm are $\Omega_i = 7$, $N_i = 3$, $h = 1$ and $sc = 0.01\%$. Fig. 3.3 highlights the steps used to compare the outputs.

The output of the proposed algorithm is compared using two different measures. I used Sum of Absolute Difference (SAD) between each $x'_i, \quad 0 \leq i \leq 3$, and x using

$$SAD(x'_i, x) = \frac{1}{m * n} \sum_{k=1}^{n} \sum_{t=1}^{m} |x'_i(k,t) - x(k,t)|. \tag{38}$$

The results for this comparison are shown in Table 3.1. The proposed algorithm outperforms the conventional interpolation methods and produce the least SAD error. Another measure for comparing the results is the Peak Signal to Noise Ratio or PSNR computed as

$$PSNR(x'_i, x) = \\ 10 \log_{10}\left(\frac{Max(x'_i) - Min(x'_i)}{\sqrt{\frac{1}{m*n}\sum_{k=1}^{n}\sum_{t=1}^{m}|x'_i(k,t) - x(k,t)|^2}}\right). \tag{39}$$

The higher PSNR implies the more accurate reconstruction of the LR image. Table 3.2 shows the

Table 3.2: Peak Signal-to-Noise Ratio (PSNR) results of proposed method versus conventional interpolation methods in dB.

Method	Patient 1	Patient 2	Patient 3	Phantom
NN	13.0904	11.5248	14.0850	11.6921
Bilinear	13.9813	11.8812	14.4330	12.2291
Bicubic	14.9000	13.0660	15.4788	13.4417
Proposed	**17.2063**	**15.5290**	**18.0046**	**15.3727**
improvement	**2.36 dB**	**2.463 dB**	**2.53 dB**	**1.85 dB**

PSNRs for different interpolations. The proposed algorithm surpasses other interpolation methods there were considered in our experiments. To present the qualitative improvement, different US images and the LR and HR counterparts obtained from different interpolation approaches are shown in Figs. 3.4 - 3.10 for patients and phantom data. The residual pattern for each interpolation and proposed method is displayed by calculating the SAD between the upsampled images and HR image. The residual patterns in each upsampled patient data using existing interpolation techniques contain substantial information from the HR image. In contrast, the SAD of the proposed algorithm is uncorrelated and does not show any pattern, which confirms the superiority of the proposed method in reconstructing the pattern of HR image.

3.5 Conclusions

In this chapter, I proposed an iterative SR approach for US imaging. The proposed method is applied to the envelope of RF data and has the ability to enhance the resolution of the image while retaining fine structures of tissue. This is demonstrated using phantom data and experiments based on *in-vivo* data. The results of the proposed algorithm are compared with interpolation approaches, which verifies the effectiveness of the proposed method. More studies are needed to fully verify the benefits of the algorithm method in US medical applications, such as US image registration and segmentation.

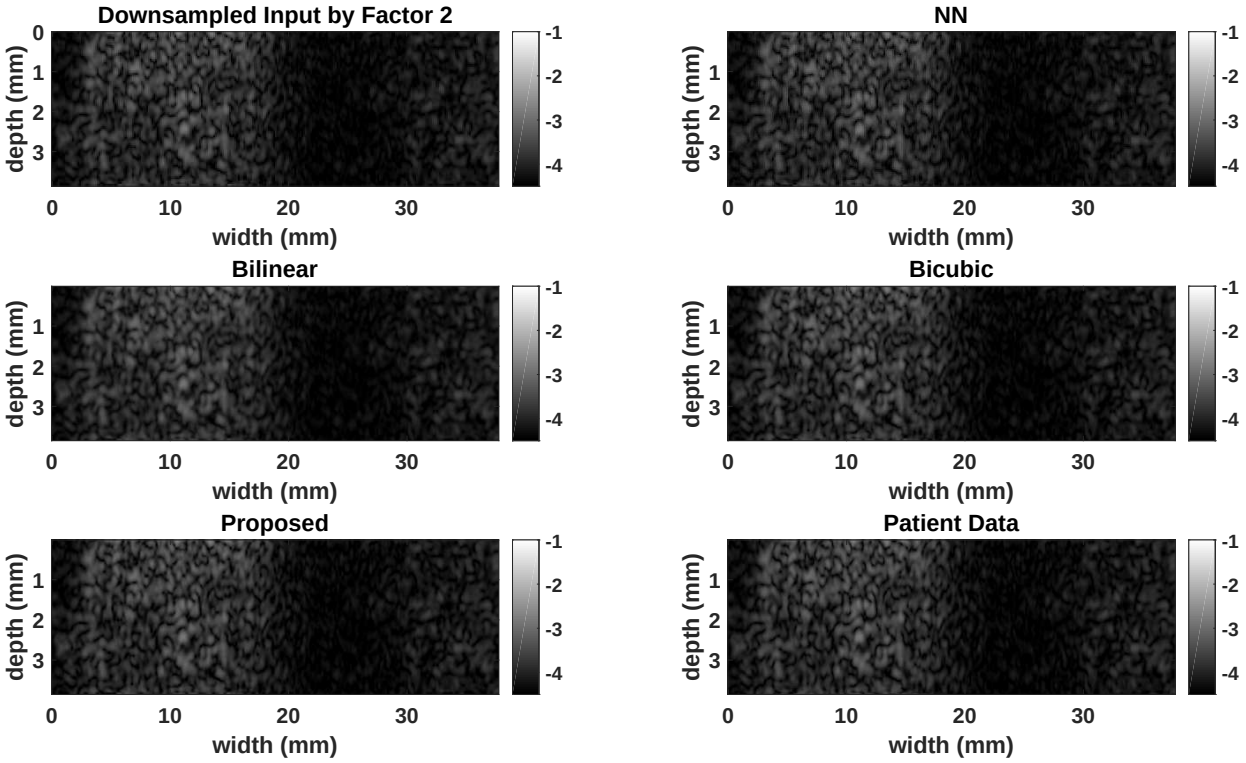

Figure 3.4: B-mode of different interpolation patient1.

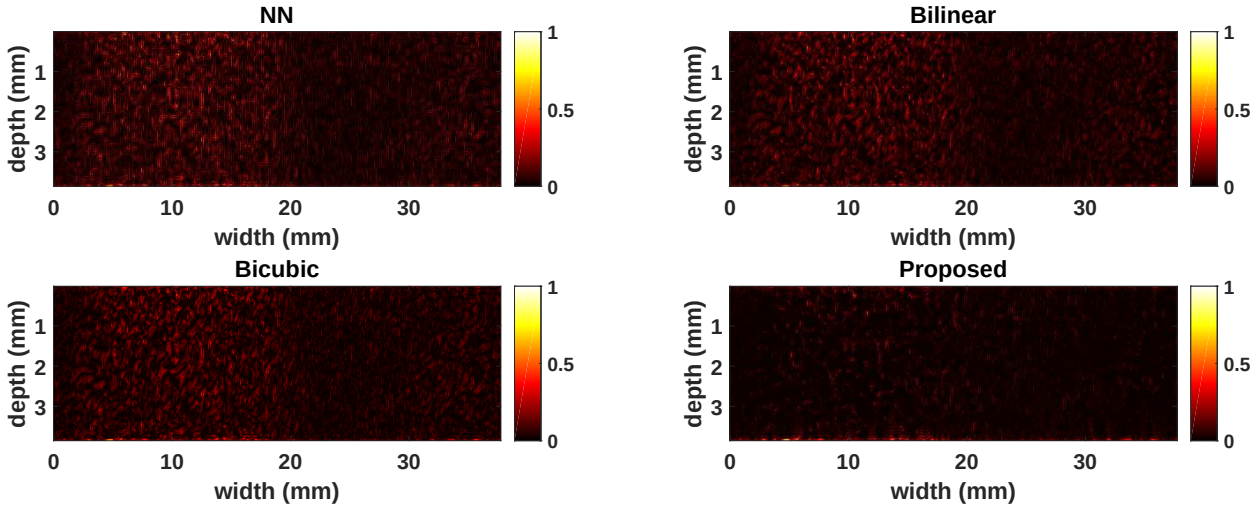

Figure 3.5: Corresponding residual patterns of patient1.

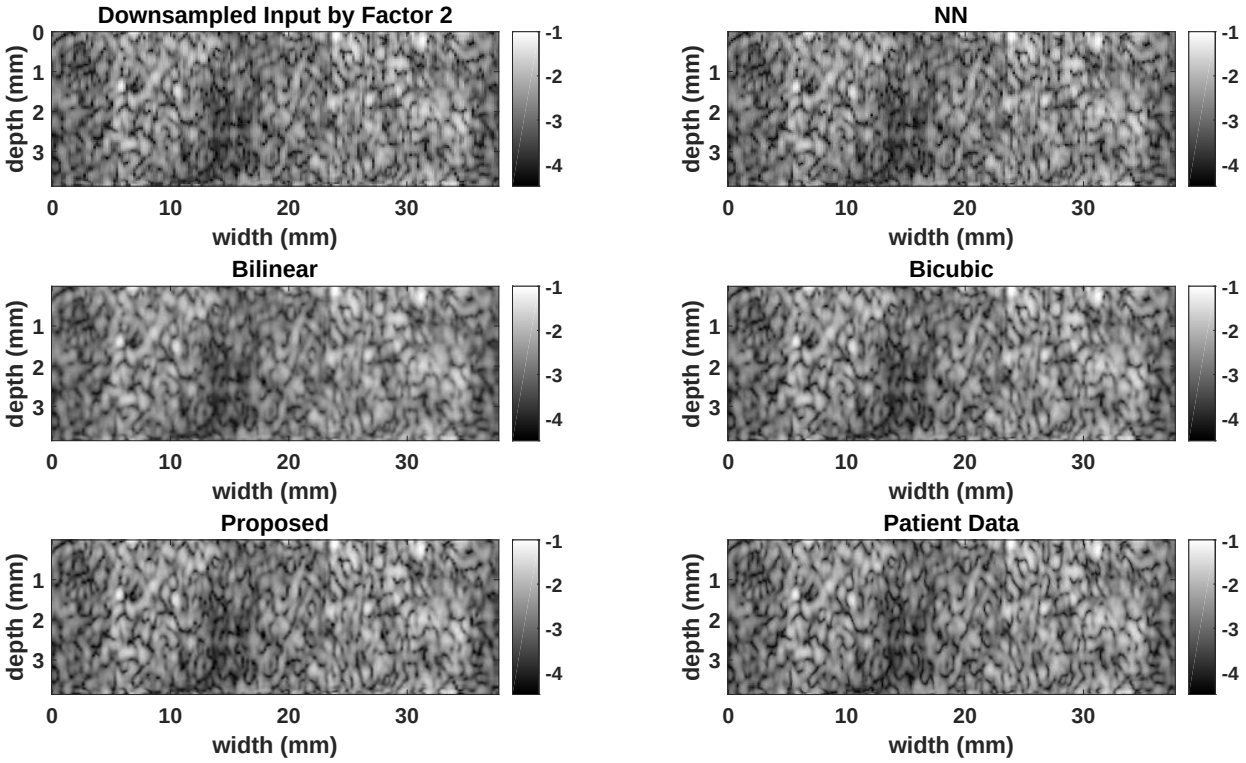

Figure 3.6: B-mode of different interpolation patient2.

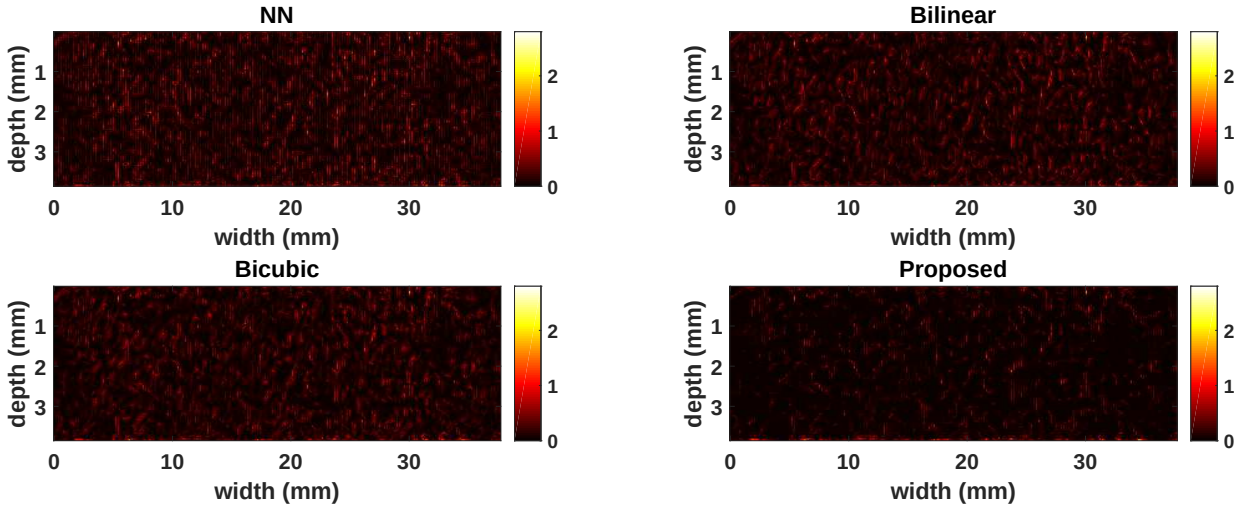

Figure 3.7: Corresponding residual patterns of patient2.

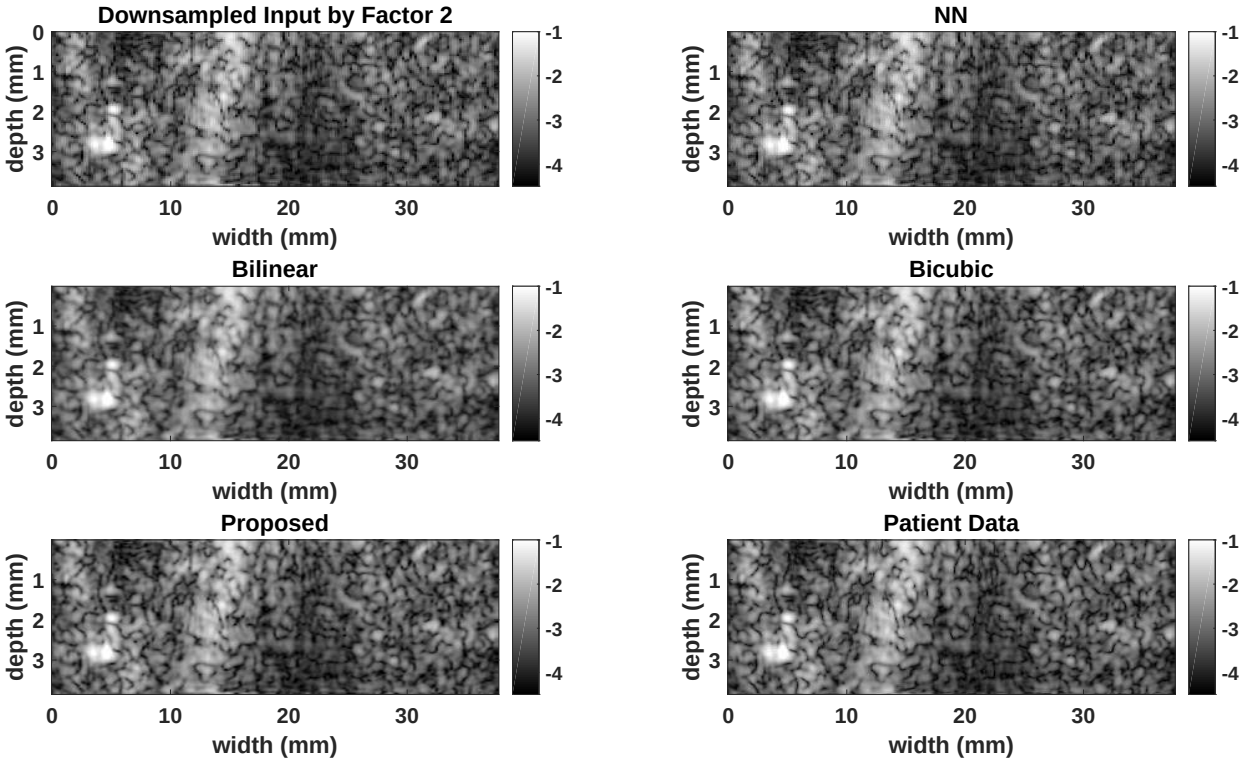

Figure 3.8: B-mode of different interpolation patient3.

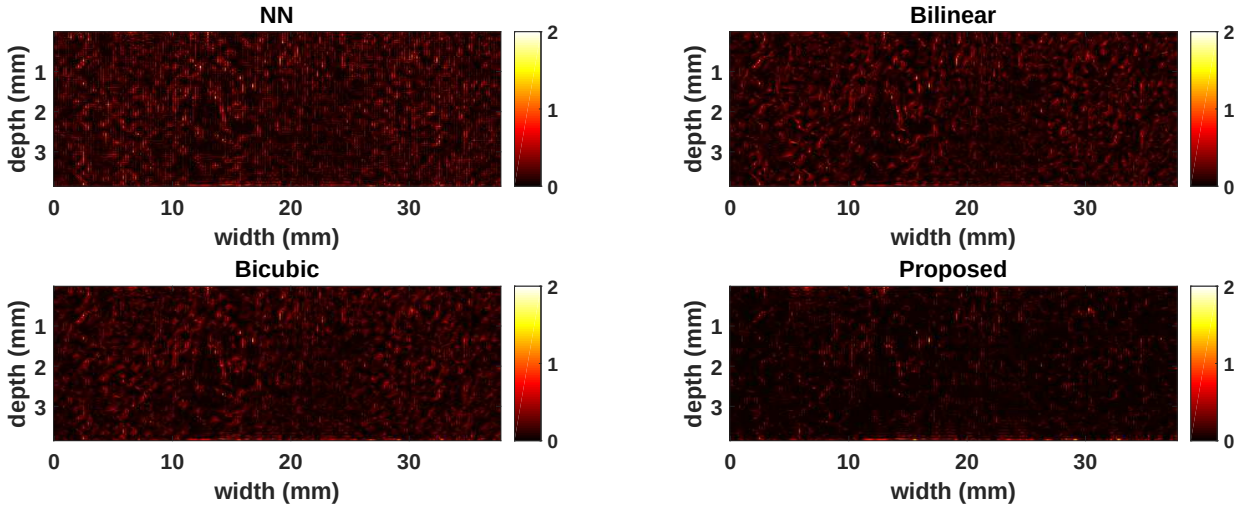

Figure 3.9: Corresponding residual patterns of patient3.

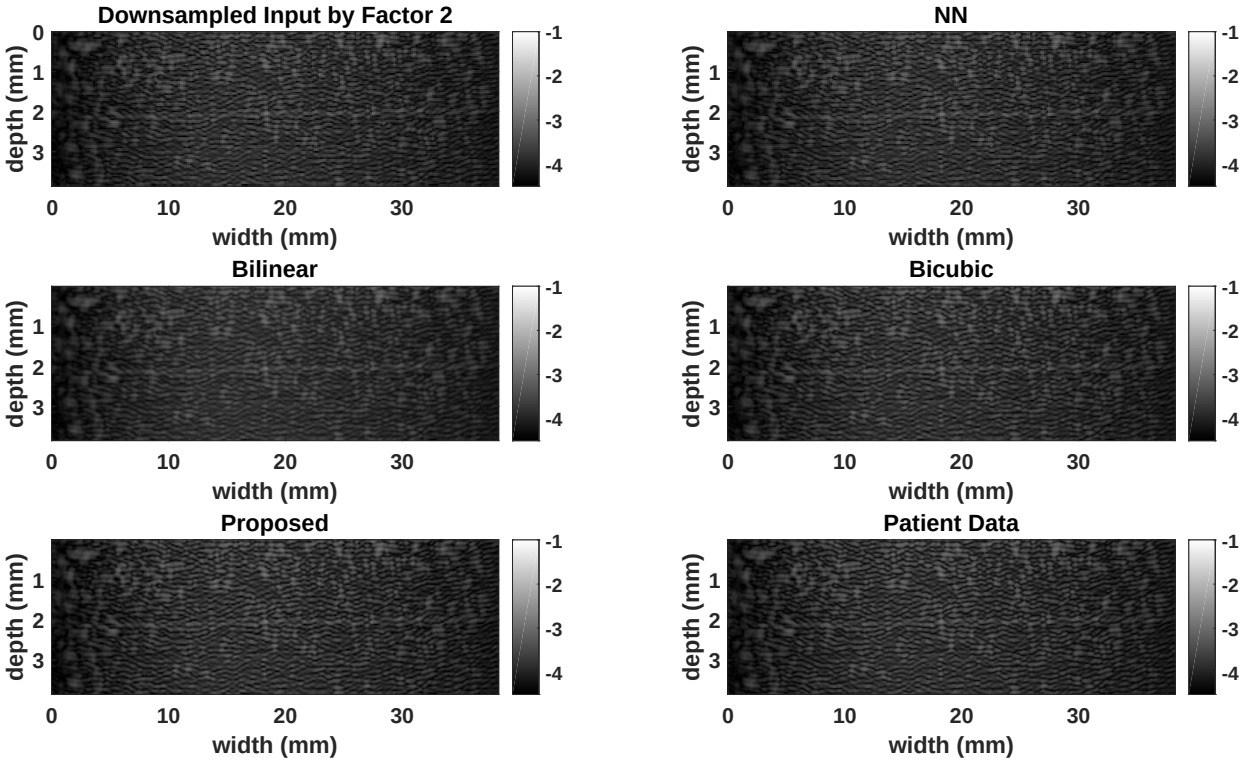

Figure 3.10: B-mode of different interpolation Phantom.

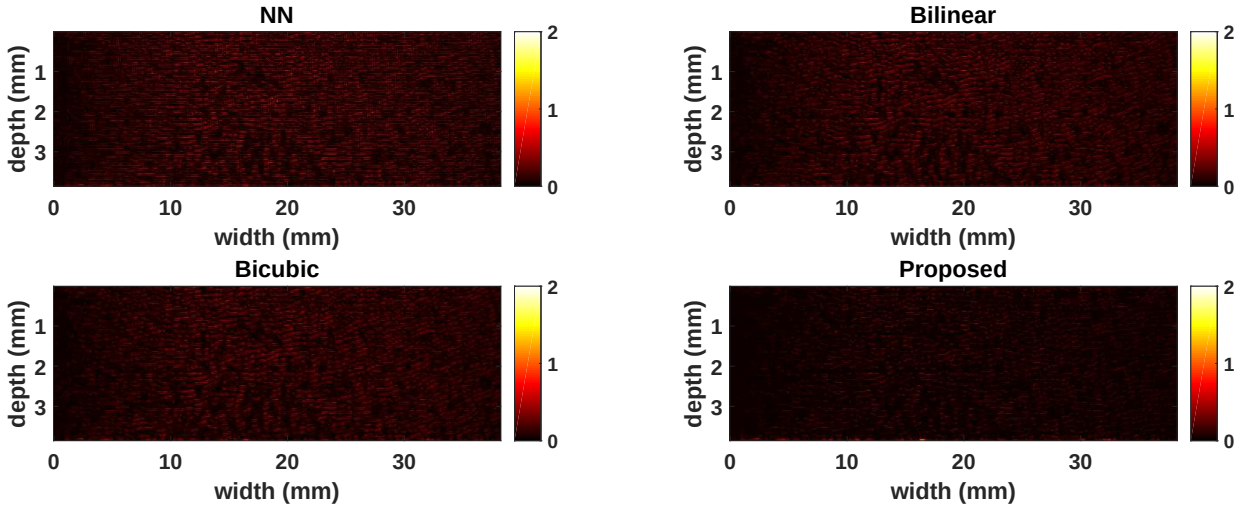

Figure 3.11: Corresponding residual patterns of Phantom.

Chapter 4

Conclusion and Future Work

4.1 Conclusions

In the first chapter of thesis, I review the basics for ultrasound and provide an overview of the thesis. I also recall the basics of ultrasound elastography and super-resolution representation to give more insights about following chapters.

In the second chapter, I present a novel non-local denoising algorithm for ultrasound elastography, CODE, that removes noise from ultrasound radio frequency data, also known as RF data, while keeps the speckles patterns constant. A Bayesian framework is proposed that studies the mathematical aspects of CODE. The performance of CODE is evaluated by comparing common quantitative parameters such as PSNR and MSE of the output of the CODE processed images. The input to CODE is a set of noisy RF field images obtained by adding noise to both synthetic data obtained from Field II as well as in-vivo data.

CODE is used for improving the performance of ultrasound elastography techniques, namely DPAM and GLUE, which are relying on the RF data of tissue for extracting the information about the mechanical properties of tissue. The aforementioned algorithms are based on optimizing a cost function using a numerical pipeline approach based on speckle pattern of RF data. At one stage of this pipeline, GLUE and DPAM are using a dynamic programming (DP) algorithm for calculation the integer displacement of the tissue. This step is vulnerable to noise. Applying CODE, GLUE and DPAM produces the strain map of the tissue without any failure. The results of CODE are compared

with other denoising methods. The performance measures in all results show the superiority of CODE in both *in-vivo* and phantom data. However, additional clinical studies are needed to perform a more comprehensive evaluation of CODE.

In ultrasound imaging, the probes with different number of piezoelectric are responsible for both transmitting and receiving the RF data. The resolution of ultrasound images has a direct relationship with number of piezoelectric and the price of probes also rises with the number of piezoelectric. ability of super-resolution methods for generating high resolution B-mode images can be used for making more affordable probes used in ultrasound machines.

In the third chapter, a novel technique for increasing the resolution of ultrasound images is proposed. The method uses non-local information in an ultrasound frame to substitute the desired pixel in enlarged image based on an iterative method using RF data. The results are compared with three conventional methods where the proposed non-local method outperforms the other approaches.

The super resolution method is tested on both *in-vivo* and phantom data with several accuracy measures. With respect to calculated residual pattern between the ground truth and enlarged images, the proposed method produce lower residual pattern in comparison with other methods. A mathematical framework is also presented in this chapter that explains the advantage of proposed method.

4.2 Future works

There are various possible ways to improve the algorithms of this thesis or transform the applications for both CODE and non-local super resolution. I have listed some of them in the followings:

- Non-local algorithms presented in chapters two and three are computationally expensive. There are several method to increase the non-local step in the both super resolution and CODE algorithms Bhujle and Chaudhuri (2014); Maruf and El-Sakka (2015); Vignesh et al. (2010). These algorithms store the repetitive computations, only compute the additional values for the non-local algorithms and can improve the proposed algorithms in this thesis to speed up.

- The proposed algorithm can be expanded to temporal domain. In this thesis, I only investigate the spatial domain of the images; however with advancements in ultrasound technologies, for

instance ultra-fast ultrasound imaging Tanter and Fink (2014) or plane-wave imaging Garcia et al. (2013), imaging in higher frame rate is now possible. With more frames, more information can be used for both CODE and non-local super resolution

- Retaining the speckles in both CODE and non-local super resolution can be used in other multimedia applications. For example ultrasound to MRI registration Rivaz et al. (2015), can use the CODE for denoising the ultrasound images and non-local super resolution for increasing the quality of ultrasound images and consequently, improving the performance of the registration.

References

Afsham, N., Najafi, M., Abolmaesumi, P., and Rohling, R. (2014). A generalized correlation-based model for out-of-plane motion estimation in freehand ultrasound. *IEEE transactions on medical imaging*, 33(1):186–199.

Banerjee, J. and Jawahar, C. (2008). Super-resolution of text images using edge-directed tangent field. In *Document Analysis Systems, 2008. DAS'08. The Eighth IAPR International Workshop on*, pages 76–83. IEEE.

Bhujle, H. and Chaudhuri, S. (2014). Novel speed-up strategies for non-local means denoising with patch and edge patch based dictionaries. *IEEE Transactions on Image Processing*, 23(1):356–365.

Buades, A., Coll, B., and Morel, J.-M. (2005). A non-local algorithm for image denoising. In *Computer Vision and Pattern Recognition, 2005. CVPR 2005. IEEE Computer Society Conference on*, volume 2, pages 60–65. IEEE.

Coupé, P., Hellier, P., Kervrann, C., and Barillot, C. (2009). Nonlocal means-based speckle filtering for ultrasound images. *IEEE transactions on image processing*, 18(10):2221–2229.

Cunningham, R. J., Harding, P. J., and Loram, I. D. (2017). Real-time ultrasound segmentation, analysis and visualisation of deep cervical muscle structure. *IEEE transactions on medical imaging*, 36(2):653–665.

Dong, C., Loy, C. C., He, K., and Tang, X. (2016). Image super-resolution using deep convolutional networks. *IEEE transactions on pattern analysis and machine intelligence*, 38(2):295–307.

Doyley, M. (2012). Model-based elastography: a survey of approaches to the inverse elasticity problem. *Physics in Medicine & Biology*, 57(3):R35.

Gao, L., Kijanka, P., Kirby, M., Pelivanov, I., Ambroziński, L., Song, S., Li, D., Yoon, S. J., Wang, R., and O'Donnell, M. (2017). Air-coupled arf-based excitation of broadband mechanical waves for dynamic elastography. In *Ultrasonics Symposium (IUS), 2017 IEEE International*, pages 1–1. IEEE.

Garcia, D., Le Tarnec, L., Muth, S., Montagnon, E., Porée, J., and Cloutier, G. (2013). Stolt's fk migration for plane wave ultrasound imaging. *IEEE transactions on ultrasonics, ferroelectrics, and frequency control*, 60(9):1853–1867.

Gennisson, J.-L., Deffieux, T., Fink, M., and Tanter, M. (2013). Ultrasound elastography: principles and techniques. *Diagnostic and interventional imaging*, 94(5):487–495.

Hamaluik, K., Moussa, W., and Ferguson-Pell, M. (2014). Numerical characterization of quasi-static ultrasound elastography for the detection of deep tissue injuries. *IEEE transactions on medical imaging*, 33(7):1410–1421.

Hashemi, H. S. and Rivaz, H. (2017). Global time-delay estimation in ultrasound elastography. *IEEE Transactions on Ultrasonics, Ferroelectrics, and Frequency Control*, 64(10):1625–1636.

Housden, R. J., Gee, A. H., Treece, G. M., and Prager, R. W. (2006). Subsample interpolation strategies for sensorless freehand 3d ultrasound. *Ultrasound in Medicine and Biology*, 32(12):1897–1904.

J Hall, T., E Barboneg, P., A Oberai, A., Jiang, J., Dord, J.-F., Goenezen, S., and G Fisher, T. (2011). Recent results in nonlinear strain and modulus imaging. *Current medical imaging reviews*, 7(4):313–327.

Jensen, J. A. (1996). Field: A program for simulating ultrasound systems. In *10th Nordicbaltic Conference on Biomedical Imaging, vol. 4, supplement 1, part 1: 351–353*. Citeseer.

Jensen, J. A. (1999). Linear description of ultrasound imaging systems: Notes for the international summer school on advanced ultrasound imaging at the technical university of denmark.

Jiang, J., Varghese, T., Brace, C. L., Madsen, E. L., Hall, T. J., Bharat, S., Hobson, M. A., Zagzebski, J. A., and Lee, F. T. (2009). Young's modulus reconstruction for radio-frequency ablation electrode-induced displacement fields: a feasibility study. *IEEE transactions on medical imaging*, 28(8):1325–1334.

Kervrann, C., Boulanger, J., and Coupé, P. (2007). Bayesian non-local means filter, image redundancy and adaptive dictionaries for noise removal. *Scale Space and Variational Methods in Computer Vision*, pages 520–532.

Khavari, P., Asif, A., Boily, M., and Rivaz, H. (2018). Nonlocal coherent denoising of rf data for ultrasound elastography. *Journal of Healthcare Engineering*, 2018.

Khodadadi, H., Aghdam, A. G., and Rivaz, H. (2015). Edge-preserving ultrasonic strain imaging with uniform precision. In *Engineering in Medicine and Biology Society (EMBC), 2015 37th Annual International Conference of the IEEE*, pages 3835–3838. IEEE.

Kortbek, J., Andresen, H., Nikolov, S., and Jensen, J. A. (2005). Comparing interpolation schemes in dynamic receive ultrasound beamforming. In *2005 IEEE Ultrasonics Symposium*, pages 1972–1975. IEEE.

Ledig, C., Theis, L., Huszár, F., Caballero, J., Cunningham, A., Acosta, A., Aitken, A., Tejani, A., Totz, J., Wang, Z., et al. (2016). Photo-realistic single image super-resolution using a generative adversarial network. *arXiv preprint*.

Lehmann, T. M., Gonner, C., and Spitzer, K. (1999). Survey: Interpolation methods in medical image processing. *IEEE transactions on medical imaging*, 18(11):1049–1075.

Maruf, G. M. and El-Sakka, M. R. (2015). Improved non-local means algorithm based on dimensionality reduction. In *International Conference Image Analysis and Recognition*, pages 43–50. Springer.

Montaldo, G., Tanter, M., Bercoff, J., Benech, N., and Fink, M. (2009). Coherent plane-wave compounding for very high frame rate ultrasonography and transient elastography. *IEEE transactions on ultrasonics, ferroelectrics, and frequency control*, 56(3):489–506.

Nasrollahi, K. and Moeslund, T. B. (2014). Super-resolution: a comprehensive survey. *Machine vision and applications*, 25(6):1423–1468.

Oelze, M. L. and Mamou, J. (2016). Review of quantitative ultrasound: Envelope statistics and backscatter coefficient imaging and contributions to diagnostic ultrasound. *IEEE transactions on ultrasonics, ferroelectrics, and frequency control*, 63(2):336–351.

Ophir, J., Alam, S. K., Garra, B., Kallel, F., Konofagou, E., Krouskop, T., and Varghese, T. (1999).

Elastography: ultrasonic estimation and imaging of the elastic properties of tissues. *Proceedings of the Institution of Mechanical Engineers, Part H: Journal of Engineering in Medicine*, 213(3):203–233.

Ophir, J., Alam, S. K., Garra, B. S., Kallel, F., Konofagou, E. E., Krouskop, T., Merritt, C. R., Righetti, R., Souchon, R., Srinivasan, S., et al. (2002). Elastography: imaging the elastic properties of soft tissues with ultrasound. *Journal of Medical Ultrasonics*, 29(4):155–171.

Ouared, A., Montagnon, E., Kazemirad, S., Gaboury, L., Robidoux, A., and Cloutier, G. (2015). Frequency adaptation for enhanced radiation force amplitude in dynamic elastography. *IEEE transactions on ultrasonics, ferroelectrics, and frequency control*, 62(8):1453–1466.

Papadacci, C., Bunting, E. A., and Konofagou, E. E. (2017). 3d quasi-static ultrasound elastography with plane wave in vivo. *IEEE transactions on medical imaging*, 36(2):357–365.

Parker, K. J., Doyley, M. M., and Rubens, D. J. (2010). Imaging the elastic properties of tissue: the 20 year perspective. *Physics in medicine and biology*, 56(1):R1.

Protter, M., Elad, M., Takeda, H., and Milanfar, P. (2009). Generalizing the nonlocal-means to super-resolution reconstruction. *IEEE Transactions on image processing*, 18(1):36–51.

Ramos-Llordén, G., Vegas-Sánchez-Ferrero, G., Martin-Fernandez, M., Alberola-López, C., and Aja-Fernández, S. (2015). Anisotropic diffusion filter with memory based on speckle statistics for ultrasound images. *IEEE Transactions on Image Processing*, 24(1):345–358.

Rivaz, H., Boctor, E. M., Choti, M. A., and Hager, G. D. (2011). Real-time regularized ultrasound elastography. *IEEE transactions on medical imaging*, 30(4):928–945.

Rivaz, H., Boctor, E. M., Choti, M. A., and Hager, G. D. (2014). Ultrasound elastography using multiple images. *Medical image analysis*, 18(2):314–329.

Rivaz, H., Boctor, E. M., and Fichtinger, G. (2006). P3e-9 ultrasound speckle detection using low order moments. In *Ultrasonics Symposium, 2006. IEEE*, pages 2092–2095. IEEE.

Rivaz, H., Chen, S. J.-S., and Collins, D. L. (2015). Automatic deformable mr-ultrasound registration for image-guided neurosurgery. *IEEE transactions on medical imaging*, 34(2):366–380.

Rivaz, H., Fleming, I., Assumpcao, L., Fichtinger, G., Hamper, U., Choti, M., Hager, G., and Boctor, E. (2008). Ablation monitoring with elastography: 2d in-vivo and 3d ex-vivo studies. *Medical Image Computing and Computer-Assisted Intervention–MICCAI 2008*, pages 458–466.

Rivaz, H., Zellars, R., Hager, G., Fichtinger, G., and Boctor, E. (2007). 9c-1 beam steering approach for speckle characterization and out-of-plane motion estimation in real tissue. In *Ultrasonics Symposium, 2007. IEEE*, pages 781–784. IEEE.

Shams, R., Xiao, Y., Hébert, F., Abramowitz, M., Brooks, R., and Rivaz, H. (2018). Assessment of rigid registration quality measures in ultrasound-guided radiotherapy. *IEEE transactions on medical imaging*, 37(2):428–437.

Stevenson, G. N., Collins, S. L., Ding, J., Impey, L., and Noble, J. A. (2015). 3-d ultrasound segmentation of the placenta using the random walker algorithm: Reliability and agreement. *Ultrasound in Medicine and Biology*, 41(12):3182–3193.

Tang, A., Cloutier, G., Szeverenyi, N. M., and Sirlin, C. B. (2015). Ultrasound elastography and mr elastography for assessing liver fibrosis: part 1, principles and techniques. *American journal of roentgenology*, 205(1):22–32.

Tanter, M. and Fink, M. (2014). Ultrafast imaging in biomedical ultrasound. *IEEE transactions on ultrasonics, ferroelectrics, and frequency control*, 61(1):102–119.

Teixeira, C. A., Mendes, L., Ruano, M. G., and Pereira, W. C. (2017). A method for sub-sample computation of time displacements between discrete signals based only on discrete correlation sequences. *Biomedical Signal Processing and Control*, 31:560–568.

Thévenaz, P., Blu, T., and Unser, M. (2000). Interpolation revisited [medical images application]. *IEEE Transactions on medical imaging*, 19(7):739–758.

Treece, G., Lindop, J., Chen, L., Housden, J., Prager, R., and Gee, A. (2011). Real-time quasi-static ultrasound elastography. *Interface focus*, 1(4):540–552.

Varghese, T., Techavipoo, U., Liu, W., Zagzebski, J. A., Chen, Q., Frank, G., and Lee Jr, F. T. (2003). Elastographic measurement of the area and volume of thermal lesions resulting from radiofrequency ablation: pathologic correlation. *American journal of roentgenology*, 181(3):701–707.

Vignesh, R., Oh, B. T., and Kuo, C.-C. J. (2010). Fast non-local means (nlm) computation with probabilistic early termination. *IEEE Signal Processing Letters*, 17(3):277–280.

Viola, F. and Walker, W. F. (2003). A comparison of the performance of time-delay estimators in medical ultrasound. *IEEE transactions on ultrasonics, ferroelectrics, and frequency control*,

50(4):392–401.

Wachinger, C., Klein, T., and Navab, N. (2012). The 2d analytic signal for envelope detection and feature extraction on ultrasound images. *Medical image analysis*, 16(6):1073–1084.

Wood, M. A., Roncalez, P., Earl, M. C. I., Van Dlac, K., Dewar, I., Roundhill, D. N., and Ungari, J. L. (1999). Ultrasonic diagnostic imaging system with data access and communications capability. US Patent 5,891,035.

Zhou, H. and Rivaz, H. (2016). Registration of pre-and postresection ultrasound volumes with non-corresponding regions in neurosurgery. *IEEE journal of biomedical and health informatics*, 20(5):1240–1249.